Multi-device study of temporal characteristics of magnetohydrodynamic modes initiating disruptions

V. Klevarová*[1], G. Verdoolaege[1], G. Pautasso[2], P.C. de Vries[3], R. Sweeney[4], T. Markovič[5,6], H. Zohm[2], M. Komm[5], J. Havlicek[5], J.A. Snipes[3], M. Lehnen[3], JET Contributors†[1], the EUROfusion MST1 team‡[1], the ASDEX Upgrade team§[1], and the DIII-D team¶[1]

[1]Department of Applied Physics, Ghent University, Sint-Pietersnieuwstraat 41, 9000 Ghent, Belgium
[2]Max-Planck-Institut für Plasmaphysik, 85748 Garching, Germany
[3]ITER organization, Route de Vinon sur Verdon, CS 90 046, 13067, St. Paul-lez-Durance, France
[4]Plasma Science and Fusion Center, MIT, 167 Albany St, Cambridge, MA 02139, USA
[5]Institute of Plasma Physics of the CAS, Za Slovankou 1782/3, 182 00, Prague, Czech Republic
[6]Faculty of Mathematics and Physics, Charles University, Prague, Czech Republic

Abstract

Disruptions in tokamaks are often preceded by magnetohydrodynamic (MHD) instabilities that can rotate or become locked to the wall. Measurements from magnetic diagnostics in the presence of MHD mode precursors to disruptions can yield potentially valuable input to the plasma control system, with a view to disruption avoidance, prediction and mitigation. This paper presents an exploratory analysis of the growth of MHD modes and corresponding time scales on the basis of magnetic measurements in multiple tokamaks. To this end, a database was compiled using disruptive discharges from COMPASS, ASDEX Upgrade, DIII-D and JET, manually classified according to disruption root cause, and characterized by a great diversity of operational conditions and mode dynamics. The typical time during which a mode can be detected using saddle coils and the duration of the locked mode phase in the database both extend over several orders of magnitude, but generally the time scales increase with plasma size. Several additional factors are discussed that can influence these durations, including the disruption root cause. A scaling law for the locked phase duration was estimated, yielding predictions toward ITER of the order of hundreds of milliseconds or even seconds. In addition, a scaling law for the mode amplitude at the disruption onset, proposed earlier by de Vries et al. (2016), is applied to the database, and its predictive capabilities are assessed. Despite significant uncertainty on the predictions from both scaling laws, encouraging trends are observed of the fraction of disruptions that may be detected with sufficient warning time to allow mitigation or even avoidance, based solely on observations of MHD mode dynamics. When combined with similar analysis of measurements from diagnostics that are sensitive to other disruption precursors, our analysis methods and results may contribute to the reliability, robustness and generalization of disruption warning schemes for ITER.

1 Introduction

Disruptions in tokamaks involve a sudden loss of the plasma confinement. They represent a potential danger to large devices through particle and heat loads on the plasma-facing components and forces applied to in-vessel structural elements [1]. A study of a large number of disruptive discharges has showed that the primary cause of the sudden decrease in the

*Corresponding author email address: veronika.klevarova@ugent.be
†See the author list of E. Joffrin et al. 2019 Nucl. Fusion 59 112021
‡See the author list of H. Meyer et al. 2019 Nucl. Fusion 59 112014
§See the author list of B. Labit et al. 2019 Nucl. Fusion 59 0860020
¶See the author list of C.C. Petty and the DIII-D Team 2019 Nucl. Fusion 59 112002

plasma energy content was a magnetohydrodynamic (MHD) mode [2]. Using measurements from magnetic diagnostics, in some cases the mode is observed to rotate, while in other cases it is static in the laboratory frame when detected. Furthermore, an initially rotating mode may be slowed down for example by interaction with surrounding conducting structures, eventually becoming locked to the wall [3]. Whereas rotation tends to have a stabilizing effect on the modes, locked modes are often seen to lead to a disruption. Therefore, in addition to the amplitude of magnetic signals caused by an MHD mode, the time from first detection of the mode to locking, and to disruption, provides important information with a view to the prediction of disruptions. Hence, the objective of the present paper is to characterize relevant mode time scales and amplitudes, as well as their dependencies across a broad range of plasma conditions in multiple devices. The dependencies are quantified by means of scaling laws, which may be interpreted in terms of known physical mechanisms. These results can be exploited for determining criteria for the design of a plasma control system (PCS) in response to MHD precursors to disruptions, discriminating between disruption root causes. In addition, while this paper does not attempt to develop a disruption predictor, our findings may constitute valuable input to disruption prediction schemes that can reliably be generalized to new devices and operational conditions.

A first line of defense against a disruption, once it is predicted, is generally referred to as disruption avoidance, wherein the PCS, continuously monitoring the plasma, acts to steer towards operational conditions with considerably lower probability for plasma disruption [4]. This can be done for instance by curing an MHD mode through application of external heating. Once the disruption cannot be avoided anymore, the PCS has to trigger actions to mitigate its effects [5]. Mitigation can consist of fast current ramp-down, accompanied by switching of the auxiliary heating, or, as a last resort, by quickly filling the vacuum chamber with gas (massive gas injection) or by injecting pellets, thereby inducing radiative collapse of the plasma.

Traditionally, disruption prediction schemes have been largely based on real-time monitoring of magnetic signals caused by locked modes. In particular, the amplitude of the locked mode signal is used for warning, as implemented in the emergency discharge shut-down schemes of several devices [6–8]. The warning threshold is typically based on experience, together with the well-known scaling with plasma current [9]. Apart from the mode lock amplitude, additional signals that are known to be related to various possible disruption causes have been used as input for more advanced disruption predictors. Various studies have shown that machine learning models can be trained to recognize, from these signals, anomalous conditions leading to a disruption [10, 11]. This has led to the implementation at several devices of machine learning disruption predictors, sometimes referred to as 'data-driven' methods, with high success rates and a low number of false positives [12–14]. However, so far it has proven a challenge to generalize these results from one operational regime to another or between devices. Nevertheless, whatever model is used to map between diagnostic signals and the disruptive probability of the plasma, generalization of disruption predictors may benefit from additional qualitative or quantitative information about the physical mechanisms underlying the development of a disruption. Such information can be provided by physical models and empirical scalings, e.g. by normalizing the monitored signals or by constraining the mapping from diagnostic signals to disruptive probability. In [9], a cross-device analysis of the locked mode amplitude at the time of disruption resulted in an empirical scaling formula for the critical mode amplitude. This scaling is applied to a multi-machine database in the present paper, with the goal of investigating its range of validity.

In addition to signals that may serve as disruption indicators, the time scales over which the MHD instability develops, locks and eventually leads to a disruption, constitutes important information for disruption avoidance, prediction and mitigation. Therefore, another goal of this paper is to characterize these time scales under various conditions and to investi-

gate what influences them. In particular, it is of interest to study under what circumstances these time scales are sufficient for timely prediction or even avoidance. Ideally, the time scales would be derived by calculating the growth rates of various types of modes [3, 15], but in practice this seems only feasible in a limited number of specific cases. Indeed, the actual mode amplitude often evolves in a complicated way, influenced by various events such as minor disruptions (accompanied by a partial loss of the plasma energy content), mode re-rotation under constant external torque input, etc. Therefore, in order to quantitatively characterize the dependencies of the duration of the mode lock phase, in this paper we resort to an approach based on empirical scaling, including uncertainty measures of the estimates.

To study the dynamics of MHD modes over a broad range of plasma conditions, in this work a multi-machine database of disruptive discharges was assembled. Devices of various sizes but (relatively) similar aspect ratio were selected (COMPASS, ASDEX Upgrade, DIII-D and JET) and the data was obtained in various operational scenarios, plasma conditions and discharge phases, with varying disruption root causes and mode dynamics. In this paper, the database is used for the following purposes:

- Conduct an exploratory cross-device analysis of mode duration and mode growth prior to disruption and identify factors that influence these characteristics.
- Derive and apply a scaling law for the duration of the locked mode phase, and extrapolate to an ITER scenario.
- Apply a scaling law for the mode amplitude at the time of disruption to the database and study its predictive capability.

The paper is structured as follows. A description of the database, including data selection and root cause classification, is given in Section 2. In Section 3, a number of factors are identified that influence the duration of the phase of mode locking. In addition, the mode growth is investigated by means of time-to-disruption curves. Furthermore, a scaling law is estimated for the locked phase duration and extrapolated to ITER. Section 4 is devoted to validation of a scaling law for the mode amplitude at the time of disruption, by means of the compiled database. A correction is proposed to better address situations where the magnetic sensors are located on the inboard side of the torus. Finally, the results are discussed and conclusions are drawn in Section 5.

2 Database compilation

A database of disruptive discharges was composed, by means of a common methodology, using data from the following tokamaks (in order of increasing plasma volume): COMPASS, ASDEX Upgrade (AUG), DIII-D and JET (ITER-like wall). The devices are of similar aspect ratio A, but differ in various other properties, such as plasma size, first wall material, etc. Some of the main device characteristics are shown in Table 1 and a list of acronyms and definitions introduced in this section can be found in Table 2.

2.1 Identification of disruptive shots

In the following, a *major disruption* is defined as a sudden drop in the plasma thermal energy content (the thermal quench), followed by a quench of the plasma current and vertical destabilization of the plasma column. During a *minor disruption* the plasma thermal content can be reduced significantly through a thermal quench as well, but the confinement is not completely lost and the plasma often recovers to its prior state. In this work, several empirical criteria were established, depending on the device, in order to recognize disruptions in a semi-automatic way. First, a device-specific threshold was set for the minimum current decay

Property	COMPASS	AUG	DIII-D	JET
Experimental period	2014–2017	2012–2016	2015	2011–2012
First wall material	C	W	C	W/Be
Minor radius a (m)	0.23	0.50	0.67	1.25
Major radius R_{geo} (m)	0.56	1.67	1.68	2.96
Aspect ratio $A = R_{\mathrm{geo}}/a$	2.4	3.3	2.5	2.4
SC location	HFS and LFS	HFS	LFS	LFS
	out and out	in	out	out
$R_{\mathrm{SC}}/R_{\mathrm{geo}}$	0.59 and 1.42	0.66	1.47	1.58
Frequency threshold f_{max} (kHz)	~ 5.0	~ 2.1	~ 0.8	~ 0.6
Resistive wall time τ_{w} (ms)	0.68 [3]	0.73 [19]	3.0 [20]	5.0 [21]
Number of database entries	252	454	150	256
RU/FT/RD (%)	6/61/33	3/30/67	3/29/68	1/14/85
ROT/IRLM/BLM (%)	50/45/5	27/54/19	21/37/42	4/54/43
Cases with $N_{\mathrm{min\ disr}} > 0$ (%)	3	79	24	81

Table 1: Main device characteristics, including location of the saddle coils (SC): high-field-side (HFS) and/or low-field-side (LFS), inside (in) or outside (out) the vacuum vessel and ratio $R_{\mathrm{SC}}/R_{\mathrm{geo}}$ of the major radius where the saddle coils are positioned (R_{SC}) over the major radius of the torus (R_{geo}). In addition, the number of database entries contributed by each device is given, as well as the fraction of disruptions in the various discharge phases (Section 2.1), the percentage of cases with characteristic mode dynamics (Section 2.2) and the fraction of shots wherein minor disruptions were observed.

characterizing a disruption, in order to discriminate disruptions from a controlled current ramp-down [16]. Another criterion for inclusion in the database was a minimum plasma current at $t = t_{\mathrm{disr}}$ of at least 35% of the (expected) current during the flat-top phase. As a result, disruptions occurring near the end of a current ramp-down, hence less dangerous cases, were excluded. Furthermore, the plasma column had to be vertically stable until the disruption onset. Hence, vertical displacement events were not studied in the scope of this work, despite their damaging potential. However, it should be noted that the physical mechanism responsible for their occurrence is well known and strategies for their prevention have been outlined [17, 18]. Cases where massive gas injection was triggered before the current quench were also excluded from the database. Furthermore, we excluded shots in which the resonant magnetic perturbation coils were operated while a mode was detected (unless for correction of intrinsic error fields in DIII-D and JET). Like that, we aimed at avoiding cases where the MHD mode field could have interfered with strong external fields. Finally, only those shots were retained for which a minimum set of plasma diagnostic data could be obtained, providing sufficient information on the mode duration and the root cause of the disruption.

The time of disruption t_{disr} was defined relative to the current spikes that are consistently observed shortly after the thermal quench. Specifically, t_{disr} was defined as the onset time of the largest current spike preceding the current quench (see Figure 1).

In several cases, minor disruptions were observed prior to the major disruption onset time t_{disr}, also accompanied by current spikes. The fraction of cases with minor disruptions is included in Table 1. Minor disruptions were rarely observed in COMPASS, but they were seen in the majority of database entries from AUG and JET. In those cases the time of the first minor disruption $t_{\mathrm{min\ disr}}$ (defined similarly as t_{disr}) was included in the database, as well as the number $N_{\mathrm{min\ disr}}$ of minor disruptions occurring during the time interval $[t_{\mathrm{min\ disr}}, t_{\mathrm{disr}}]$. If no minor disruptions were observed prior to t_{disr}, then $t_{\mathrm{min\ disr}} = t_{\mathrm{disr}}$ and $N_{\mathrm{min\ disr}} = 0$.

BLM	Born-locked mode
FT	Plasma current flat-top
IRLM	Initially rotating locked mode
RD	Plasma current ramp-down
ROT	Rotating mode
RU	Plasma current ramp-up
Δt_{LP}	Locked phase duration
Δt_{SC}	Saddle coil signal duration
$N_{\mathrm{min\ disr}}$	Number of minor disruptions
t_{disr}	Disruption time
$t_{\mathrm{min\ disr}}$	First minor disruption time
t_{SC}	Saddle coil signal onset time

Table 2: List of selected acronyms and definitions.

2.2 Detection of rotating and locked MHD modes

Once a discharge was labeled as disruptive, data from diagnostics sensitive to MHD modes, both rotating and locked, was investigated. For rotating modes, the rotational phase was identified using spectrograms detected by fast sampling Mirnov coils sensitive to the poloidal field component of the mode, and the rotation frequency f was tracked in time. The mode structure in terms of the toroidal mode numbers n (in AUG also the poloidal mode number m) was resolved by analysis of the cross-phase.

Detection of locked modes was done using two pairs (three in DIII-D) of saddle coils (SC), their geometrical centre located at a major radius R_{SC}, separated by a toroidal angle $\pi/2$ ($\pi/3$). The mode amplitude B_{r}, i.e. the associated radial component of the magnetic field, can then be calculated as a squared sum of differences of fluxes Φ detected by opposing coils. For j coils located at toroidal angles ϕ_{j}, one can formulate the calculation in terms of a least square fit in matrix form,

$$\begin{pmatrix} \sin(\phi_1)-\sin(\phi_2) & \cos(\phi_1)-\cos(\phi_2) \\ \sin(\phi_3)-\sin(\phi_4) & \cos(\phi_3)-\cos(\phi_4) \\ \vdots & \vdots \\ \sin(\phi_{\mathrm{j}-1})-\sin(\phi_{\mathrm{j}}) & \cos(\phi_{\mathrm{j}-1})-\cos(\phi_{\mathrm{j}}) \end{pmatrix} \begin{pmatrix} a \\ b \end{pmatrix} = \begin{pmatrix} \Phi(\phi_1)-\Phi(\phi_2) \\ \Phi(\phi_3)-\Phi(\phi_4) \\ \vdots \\ \Phi(\phi_{\mathrm{j}-1})-\Phi(\phi_{\mathrm{j}}) \end{pmatrix}, \tag{1}$$

where a and b are the amplitudes of the $n = 1$ sine and cosine components, respectively, and coil '1' is opposite to coil '2', coil '3' opposite to coil '4' etc. For a detector composed of four saddle coils, displaced by $\pi/2$ with respect to each other, the calculation of the mode amplitude reduces to

$$B_{\mathrm{r}} = \frac{c}{2}\sqrt{\Big[\Phi(\phi_1)-\Phi(\phi_2)\Big]^2+\Big[\Phi(\phi_3)-\Phi(\phi_4)\Big]^2} = c\sqrt{a^2+b^2}. \tag{2}$$

The factor c depends on the coil geometry and relates to the conversion of magnetic flux to field strength. The mode phase θ is obtained as the inverse tangent of the flux ratio,

$$\theta = \arctan\left[\frac{\Phi(\phi_1)-\Phi(\phi_2)}{\Phi(\phi_3)-\Phi(\phi_4)}\right]. \tag{3}$$

In AUG the coils are located inside the vacuum vessel, whereas in the other devices they are positioned outside the vessel (Table 1). The measured signal variations are influenced by the characteristic resistive vessel time τ_{w}. The measured $\mathrm{d}B_{\mathrm{r}}/\mathrm{d}t$ signal is integrated by hardware that acts as a low-pass filter with a device-specific upper detectable frequency

$f_{\max}$ (Table 1). In practice, this means that the locked mode detector can only recognize modes rotating at frequency $f < f_{\max}$. In fact, the time during which the B_r signal can be distinguished from noise has occasionally been referred to as the *locked mode duration* in the literature, whereas in reality it may comprise part of a mode's rotational phase. Nevertheless, locked modes can be more easily detected by the saddle coils than rotating ones, since a rotating mode induces currents in the surrounding resistive wall, attenuating the mode's radial field [22]. For this reason, it is important to note that, for modes rotating prior to locking, the measured amplitude does not necessarily match the actual radial field component of the mode.

To avoid misleading terminology, here we define the saddle coil signal onset time t_{SC} as the time at which the measured B_r due to the mode surpasses the noise level. A *saddle coil signal duration* $\Delta t_{SC} = t_{disr} - t_{SC}$ can also be calculated. This is indicated in Figure 1, which shows an example of a discharge in AUG with an initially rotating $m/n = 3/1$ mode of vanishing amplitude, followed by an initially rotating 2/1 mode that ultimately disrupted the plasma. Inspection of the time variation of the 2/1 mode phase (shown in the third panel) allows to delimit the mode rotation and locked phases by the instant from which the phase variation is small. This time point defines the mode locked phase onset t_{LP}. The slight variation of the phase, observable in the example, indicates, strictly speaking, quasi-stationarity. Impacts of the mode quasi-stationarity on the analysis presented in this paper is minor and it is therefore neglected in the definition of a *locked phase duration* Δt_{LP}, defined as the time interval from the moment when the mode becomes (quasi-)stationary until disruption onset, $\Delta t_{LP} = t_{disr} - t_{LP}$. In COMPASS, the mode phase was not calculated, therefore the locked phase refers to the time interval where the poloidal component of the mode field, detected by the Mirnov coils, exhibits no oscillations. In addition, at COMPASS two sets of saddle coils were used for mode detection, one set located at the low-field-side (LFS) and another at the high-field-side (HFS) of the torus.

The database entries were divided in groups defined according to the mode dynamics:

ROT Modes (slowly) rotating until the major disruption onset, and accordingly with $\Delta t_{LP} = 0$.

IRLM Initially rotating modes that eventually locked, with $\Delta t_{SC} > \Delta t_{LP}$, $\Delta t_{LP} > 0$.

BLM Born-locked modes, with $\Delta t_{SC} = \Delta t_{LP}$.

The relative occurrence of the database entries in these groups is listed in Table 1, for the four devices. For increasing plasma size, there appears to be a shift from purely rotating modes to modes with a locking phase, and eventually to a sizeable fraction of born-locked modes in the largest devices.

From the above it is clear that in all database entries $\Delta t_{SC} > 0$. In Section 3.1, this time interval will be used as a measure of the mode duration and multiple factors that can influence this time interval will be discussed therein. Regression analysis of the duration will be restricted in Section 3.2 to cases with $\Delta t_{LP} > 0$, as this time interval is assumed to be less influenced by the diagnostic-dependent settings.

2.3 Summary of the database

The applied selection criteria led to a database with in total 1 100 disruptive discharges. Table 1 shows the number of database entries for the various devices, as well as their distribution over the various discharge phases: current ramp-up (RU) phase, flat top (FT) and ramp-down (RD) phase (whether intentional or as a consequence of disruption precursors). It can be seen that only in the case of the COMPASS device, the majority of disruptions took place during the current flat-top phase, whereas in the other devices most disruptions in the database occurred during current ramp-down.

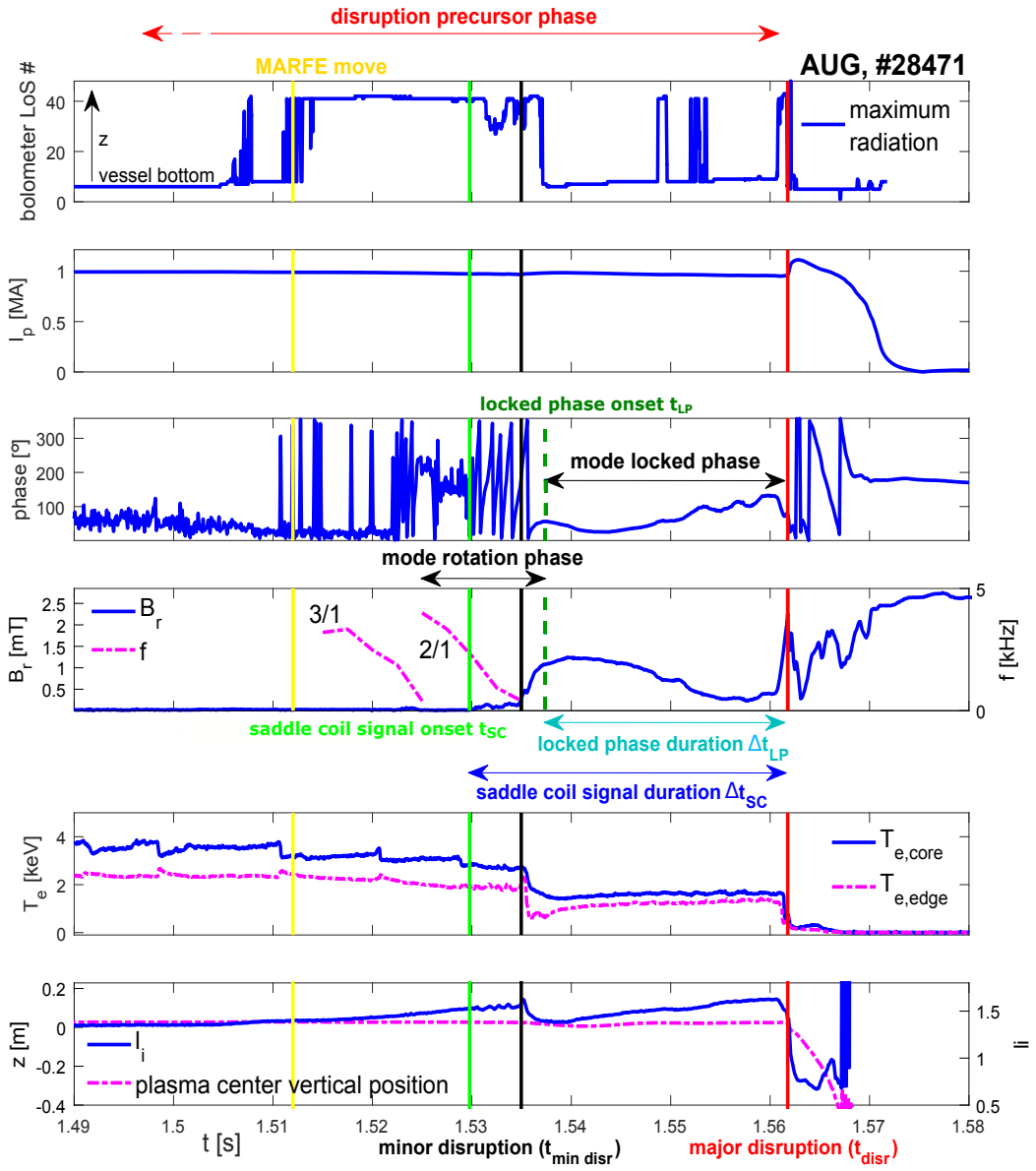

Figure 1: Example of an initially rotating locked mode (an IRLM case at AUG) disrupting the plasma at $t = t_{\mathrm{disr}}$. The disruption precursor phase is highlighted, with poloidal displacement of a MARFE from its stable location at the X-point and sequential onset of initially rotating 3/1 and 2/1 modes. The radial component B_{r} of the mode field surpasses the noise level at $t = t_{\mathrm{SC}}$, determining the starting point of the *saddle coil signal duration* Δt_{SC}. The mode phase is roughly constant during a time interval Δt_{LP}, defining the *locked phase duration*.

Parameter	Symbol	COMPASS	AUG	DIII-D	JET
Magnetic major radius	R_{mag} (m)	0.56 ± 0.01	1.68 ± 0.02	1.73 ± 0.03	2.94 ± 0.02
Elongation	κ	1.73 ± 0.28	1.60 ± 0.08	1.75 ± 0.12	1.65 ± 0.07
		1.75 ± 0.28	1.55 ± 0.10	1.64 ± 0.14	1.46 ± 0.15
Lower triangularity	δ_{l}	0.50 ± 0.20	0.35 ± 0.04	0.48 ± 0.14	0.32 ± 0.06
		0.48 ± 0.19	0.33 ± 0.04	0.36 ± 0.19	0.18 ± 0.10
Plasma current	I_{p} (MA)	0.17 ± 0.05	0.79 ± 0.30	1.06 ± 0.18	1.90 ± 0.21
		0.16 ± 0.05	0.74 ± 0.28	0.94 ± 0.18	1.64 ± 0.29
Toroidal magnetic field	B_{t} (T)	1.17 ± 0.08	2.47 ± 0.18	1.93 ± 0.23	2.18 ± 0.26
Internal inductance	l_{i}	1.08 ± 0.05	1.44 ± 0.27	1.07 ± 0.38	1.18 ± 0.19
		1.07 ± 0.15	1.74 ± 0.34	1.53 ± 0.51	1.31 ± 0.10
Edge safety factor	q_{95}	3.55 ± 0.79	4.73 ± 0.63	4.03 ± 0.75	3.42 ± 0.48
		3.53 ± 0.78	4.77 ± 0.64	4.08 ± 0.82	3.88 ± 0.60
Normalized beta	β_{N} (%)	1.07 ± 0.28	0.50 ± 0.33	0.67 ± 0.52	0.20 ± 0.12
		0.91 ± 0.26	0.36 ± 0.18	0.40 ± 0.50	0.26 ± 0.10
Poloidal beta	β_{pol} (%)	0.58 ± 0.20	0.26 ± 0.20	0.28 ± 0.39	0.09 ± 0.05
		0.44 ± 0.17	0.15 ± 0.13	0.13 ± 0.39	0.13 ± 0.06
NBI input power	P_{NBI} (MW)	0.25 ± 0.06	4.91 ± 2.61	3.78 ± 2.34	2.13 ± 3.05
		0.25 ± 0.06	4.89 ± 2.47	3.50 ± 1.90	1.81 ± 3.08
Density (core)	n_{e} ($10^{19}\mathrm{m}^{-3}$)	5.21 ± 3.02	6.33 ± 3.77	2.90 ± 1.94	3.67 ± 1.58
		5.09 ± 2.85	5.96 ± 2.49	2.71 ± 1.58	2.07 ± 1.29
Temperature (core)	T_{e} (keV)	0.65 ± 0.23	0.97 ± 0.78	1.53 ± 0.66	0.77 ± 0.58
		0.62 ± 0.22	0.34 ± 0.45	1.50 ± 0.68	0.41 ± 0.21

Table 3: Summary of the data contributed by each device, in terms of the median and median absolute deviation over the database, for each device. The data were collected at the two time instants t_{SC} (first line for each parameter) and t_{disr} (second line, not shown for medians differing less than 10%).

For each discharge in the database, a number of plasma parameters was obtained at the two time instants $t = t_{\mathrm{SC}}$ (mode detection) and $t = t_{\mathrm{disr}}$ (disruption onset). A selection of these parameters is summarized in Table 3 by means of the median value over the database, accompanied by the median absolute deviation (MAD) as a measure of dispersion. The median was preferred over the mean because some of the parameter distributions were considerably skewed, heavy-tailed or multimodal (see below). The plasma density and temperature were mostly obtained from the plasma core region.

2.4 Disruption classification

A large set of disruptive discharges in JET was investigated in detail in [2] (carbon wall) and [23] (ITER-like wall), with the goal of describing the chain of events leading to the disruption, and in particular the root cause. The classification was adopted and further developed for AUG [24]. A similar classification was applied to the database developed in this work [2, 22–29]. The various classes are briefly described in Table 4 and the distribution of the database entries over the classes is given. The classification was done manually on the basis of time traces of various plasma parameters and images from fast cameras. The location of the discharge in the l_{i}–q_{95} diagram at t_{disr} is particularly informative [24, 30]. Current-driven instabilities, typically triggered when a density limit is approached, tend to be located in a region of highly peaked current profiles (high l_{i}), while the pressure-driven instabilities, such as neoclassical tearing modes (NTMs), usually exhibit a rather flat current profile.

The relative occurrence of the classes is quite different in each of the devices. It can be

influenced by several factors, such as the first wall material, type and level of vacuum vessel conditioning, dust inventory, impurity gas puffing, etc. Naturally, the experimental program itself also affects the distribution of disruption classes, as well as the specific response of the PCS to exceptional events. We list here the main observations regarding disruption class prevalence:

COMPASS In COMPASS, MHD precursors serving as seeding islands for NTMs were regularly observed in the database, owing to the generally high β. On the other hand, most of the COMPASS shots in our database have pure Ohmic heating, therefore rather few disruptions are included that are due to switching off neutral beam heating. In addition, the fraction of born-locked modes is quite low because the intrinsic error field is weak and at the same time the plasma tends to rotate strongly [31].

AUG Divertor detachment is often achieved in AUG. Experiments on detachment show a high disruptivity due to the need for high plasma density and injection of impurities. A poloidal destablization of MARFE from its location close to the plasma X-point can cause growth of the MHD modes.

DIII-D This machine operates relatively often at a low q_{95}, thus approaching the ideal MHD disruption limit. Hence, quite a number of (intentional) ideal β limits were identified in this device. Furthermore, as the plasma density in DIII-D can also be rather low, many disruptions were seen in the category of born-locked modes excited by error fields (quite strong in DIII-D [32]), often in the early phase of the discharge.

JET In JET, as in AUG, divertor detachment is a relatively common cause of disruption. In addition, similar to DIII-D, a large fraction of modes was of the born-locked type. Indeed, as opposed to COMPASS, large devices with presumably little plasma rotation [33] are quite vulnerable to this type of disruptions. This points at the necessity of error field correction in ITER [34]. Furthermore, a substantial fraction of disruptions was caused by impurity accumulation in the core (this was pointed out in [23]).

Finally, in the study of JET disruptions it was found that the root cause of a large part of the disruptions was related to technical failures (e.g. issues with density control) [2]. It is likely that this is also the case for a significant number of disruptions obtained from the other devices in this study. However, this is not considered in more detail here, as we assume that the mode growth does not depend on whether the observed root cause can be tracked back to a technical fault.

3 Time scales of MHD modes leading to disruptions

Analysis of mode dynamics can provide very useful information for disruption avoidance and prediction. The database compiled in this work can be exploited to that end by investigating the time scales of mode growth and locking, as well as their parametric dependencies. In this study, we analysed the saddle coil signal duration Δt_{SC} and the locked phase duration Δt_{LP}.

3.1 Saddle coil signal duration Δt_{SC}

Ideally, the dependence of the mode growth rate on plasma parameters would be determined from first principles, resulting in an analytical expression for the mode duration. In our work, the saddle coil signal duration Δt_{SC} may serve as a measure of mode duration for all database entries given that $\Delta t_{\mathrm{SC}} > 0$ in all cases. This duration is determined by a multitude of factors related to the plasma conditions, as well as characteristics of the device and the saddle coils. Investigating mode growth during this period is often complicated

Class code	Description	Occurrence in COMPASS/AUG/ DIII-D/JET (%)
ACC	Impurity accumulation in the core, resulting in localized cooling and conditions favourable for destabilization of MHD modes.	4/12/0/32
BLIM	An ideal MHD instability, typically encountered when β approaches the Troyon limit.	5/<1/11/0
DL	MHD modes driven unstable (in L-mode or after exiting the H-mode) when the plasma density approaches the Greenwald density limit. Poloidal destabilization of a MARFE may contribute to the mode onset.	<1/53/15/25
IMP	Too high impurity levels leading to excessive radiative losses, triggering MHD modes.	8/12/<1/17
LON	Born-locked modes excited due to device error fields. Common risk factors are a low plasma density and low q_{95}.	<1/2/11/13
LOQ	An ideal MHD limit, associated to $q_{95} \to 2$.	4/0/5/2
NBIOFF	Turning off the auxiliary NBI heating close to the density limit and/or in the presence of high impurity levels can destabilize MHD modes.	2/7/13/5
NTM	Initially quasi-stable or short living neoclassical tearing modes driven unstable at high plasma β.	67/8/22/5
RU	Too fast a current ramp-up (resulting in a flat current density profile) and near-rational q_{95} can lead to MHD mode onset.	9/6/22/1

Table 4: Disruption classification: class code, brief description of the disruption class and, for each device, the relative occurrence of the class in the database compiled in the present work.

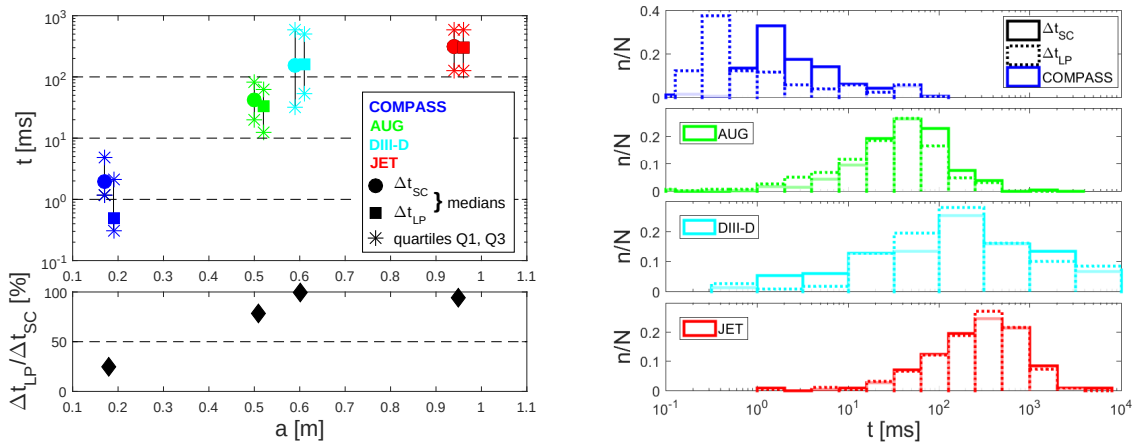

(a) (b)

Figure 2: (a) Median Δt_{SC} and Δt_{LP} (upper panel) and their ratio $\Delta t_{\mathrm{LP}}/\Delta t_{\mathrm{SC}}$ (lower panel) versus minor radius a in the four devices. The error bars indicate the first and third quartiles of the distributions shown in (b).

by fluctuations in the B_{r} signal. Only in a small subgroup of discharges (typically error field locked modes or modes growing on the fastest time scale for each device), the mode amplitude evolves without fluctuations. There can be various reasons for such fluctuations, like radial motion of the mode with respect to the detection instruments, varying mode size due to a minor disruption, lack of free energy supporting the mode growth, increase in the mode rotation rate etc. Because of such complications, the discussion of Δt_{SC} is limited here to a number of phenomenological observations. We also construct *time-to-disruption curves* for the four devices in the database. These curves provide information on the typical time scales available for the PCS to react to MHD modes, from the time of detection by the saddle coils. The action may be aimed at avoiding a disruption due to the mode or it may involve mitigation of a disruption, if it can no longer be avoided. The decision as to which action is appropriate should be based on a risk assessment that takes into account the probability of a false positive identification of an impending disruption, but this assessment is outside the scope of the present paper. Rather, our exploration of Δt_{SC} across the database is intended to provide information about upper limits on the attainable prediction time, as well as the variation among devices. This may serve as an input to the PCS for determining the appropriate action in response to the observed disruption precursors.

3.1.1 Dependence of Δt_{SC} on plasma size

One of the clearest factors influencing the saddle coil signal duration Δt_{SC} was found to be the plasma size, measured here by the plasma minor radius a. In Figure 2a (upper panel), the median Δt_{SC} is plotted for each device against a. For COMPASS, the data were obtained from the set of coils on the LFS. There appears to be an increasing trend of the time scale with a. However, while the median time scales exhibit a clear trend, it should be mentioned that the distribution of Δt_{SC} is relatively broad and skewed, as shown in Figure 2b (see also Tables 5 and 6). Nevertheless, the overall trend is favorable for large devices such as ITER. A similar trend of Δt_{LP} with a will be discussed in Section 3.2.

It should be kept in mind that, as with all dependencies noted here, the concurrent variation of other parameters in addition to the plasma size (e.g. relative occurrence of disruption classes), contributes to the uncertainty in the observed dependence. This is also why in Section 3.2 a scaling law is proposed for Δt_{LP} to disentangle the different effects.

Class code	COMPASS	AUG	DIII-D	JET
ACC	2.2, **2.6**, 5.5	9.1, **36**, 77	–, –, –	316, **477**, 738
BLIM	0.8, **1.2**, 2.9	–, **1.7**, –	2.6, **12**, 55	–, –, –
DL	–, **0.94**, –	31, **48**, 82	7.5, **53**, 141	128, **175**, 290
IMP	0.7, **1.0**, 1.6	5.8, **15**, 20	–, **8.2**, –	49, **101**, 415
LON	–, **4.4**, –	106, **151**, 255	87, **198**, 363	461, **679**, 971
LOQ	0.1, **0.8**, 1.6	–, –, –	–, **32**, –	–, **99**, –
NBIOFF	–, **3.8**, –	42, **62**, 87	58, **121**, 168	87, **97**, 191
NTM	1.3, **1.9**, 4.3	9.8, **27**, 116	227, **822**, 1 700	136, **231**, 801
RU	7.2, **20**, 37	14, **62**, 134	162, **401**, 4 400	–, **254**, –

Table 5: Intervals Δt_{SC} (ms) for the four devices in each of the disruption classes. The median values are shown in bold, as well as the first and third quartile over the database.

3.1.2 Dependence of Δt_{SC} on disruption class

Another important source of variation of Δt_{SC} is the root cause of the disruption. This is summarized in Table 5, using the categories defined in Table 4. Relatively speaking in each of the devices, the longest mode durations are found in the LON and RU classes, while in DIII-D and JET the NTM class also exhibits long time intervals, as does the ACC class in JET. On the other hand, modes in the IMP, BLIM and LOQ groups overall have the shortest durations, with the latter two related to fast growth of ideal MHD instabilities. Naturally, the greatly varying time scales depending on disruption class, combined with the different relative occurrence of disruption classes over the four devices (Table 4) contributes to the width of the time scale distributions in Figure 2b.

3.1.3 Effect of emergency current ramp-down on Δt_{SC}

As mentioned before, various technical issues or failures can indirectly lead to disruptions. Likewise, the way the PCS reacts to disruption precursors also influences the duration of observation of MHD modes using the saddle coils. One operational characteristic that clearly puts a limit on Δt_{SC} in a relatively large fraction of database entries from AUG (30%) and JET (77%) is an emergency current ramp-down (E-RD) (in DIII-D less then 5%). This can be initiated by the PCS, e.g. in response to the detection of a large mode amplitude [6, 8]. It is a common first action toward emergency discharge shut-down aiming at disruption mitigation at larger plasma current. Other actions include switching off part of the auxiliary heating and, eventually, massive gas injection or pellet injection.

The most apparent influence of E-RDs is seen in the median Δt_{SC}, which in AUG is 35 ms for the group of discharges with E-RD and 72 ms without. In JET, the median Δt_{SC} is 101 ms with E-RD and 385 ms without, so an E-RD clearly causes the mode to shrink below the detection limit. From a physics point-of-view, an E-RD lowers the l_{i}/q_{95} ratio associated with the free energy supporting the mode growth [35]. Lowering of the ratio is presumably linked to the increase in q_{95} induced by the decrease in the plasma current.

The main point here is that it is important to keep in mind that the time scales of mode evolution in the database can be limited by several operational factors. This means that there is probably a substantial fraction of cases in the database where the actual time to the disruption, hence the time available for the PCS to act upon a disruption, could have been longer with different operational choices made.

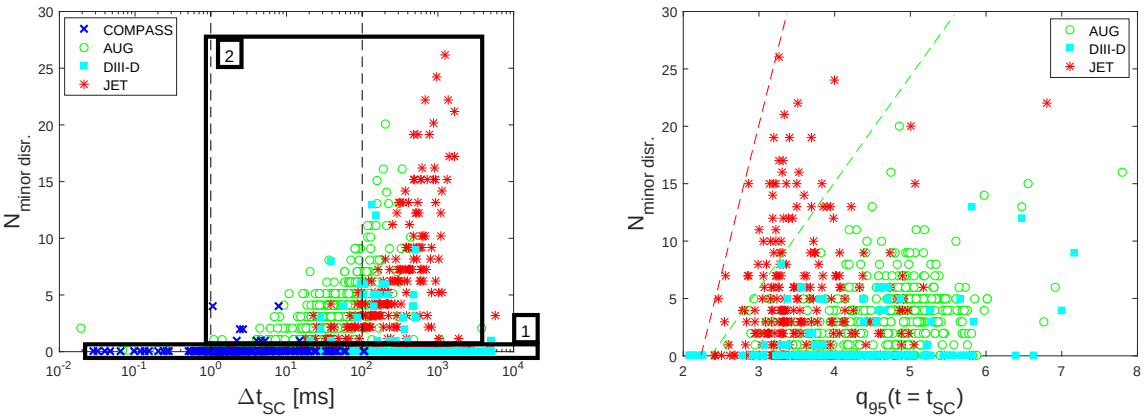

(a) (b)

Figure 3: (a) Number of minor disruptions $N_{\text{min disr}}$ preceding the major disruption onset, plotted against Δt_{SC}. (b) $N_{\text{min disr}}$ versus q_{95}.

3.1.4 Relation between Δt_{SC} and minor disruptions

The occurrence of minor disruptions can result in a complex mode growth scenario. The relative occurrence of shots in our database where minor disruptions were produced before the major disruption has been shown in Table 1. Figure 3a shows a plot of the number of minor disruptions $N_{\text{min disr}}$ against Δt_{SC} for the four devices. As expected, for a large number of cases (group '2'), the longer the mode is observed until the time t_{disr} of the major disruption, the larger $N_{\text{min disr}}$. However, there is a sizeable number of shots (group '1') without any minor disruption prior to t_{disr}. Further analysis revealed that the majority of discharges within group 2 are of the type DL, NBIOFF, ACC or IMP, whereas group 1 is mainly populated by BLIM, LOQ and LON types (see also [36, 37]). A link between $N_{\text{min disr}}$ and the mode dynamics (ROT, IRLM or BLM) could not be found.

Figure 3b displays $N_{\text{min disr}}$ as a function of q_{95} at t_{SC} for AUG, DIII-D and JET (most COMPASS shots are in group 1). Discharges with minor disruptions occur for a broad range of safety factors, but nevertheless the database allows establishing upper limits on $N_{\text{min disr}}$ (visualized by dashed lines in the figure) for a given q_{95}. A weakly decreasing trend of $N_{\text{min disr}}$ versus l_{i}/q_{95} was found as well.

It is also of interest to note that, whereas minor disruptions do not pose any danger in present-day devices, in future larger devices the thermal energy loss during minor disruptions might be sufficient to cause damage to the plasma-facing components. Under these circumstances, disruption avoidance and prediction schemes may also need to account for these minor disruption events. We therefore briefly examine the available time between the saddle coil onset time t_{SC} and the time of the first minor disruption: $\Delta t_{\text{SC,min}} = t_{\text{min disr}} - t_{\text{SC}}$. This interval is compared to Δt_{SC} in Table 6 for the four devices. As expected, the available time to the first minor disruption can be significantly shorter (by a factor ranging from ~ 2 to 17) than the time to the major disruption, particularly in those devices where minor disruptions are relatively common.

3.1.5 Mode growth and time to disruption

Having established several important sources of variability of Δt_{SC}, we now systematically investigate the time to disruption (TtD) from the point where the mode amplitude, as measured by the saddle coils, exceeds a certain threshold. Our database allows studying the variability of the TtD, for multiple threshold levels, in each device and between devices.

Interval	COMPASS	AUG	DIII-D	JET
$\Delta t_{\mathrm{SC}} = t_{\mathrm{disr}} - t_{\mathrm{SC}}$ (ms)	$1.2, \mathbf{2.0}, 4.9$	$20, \mathbf{42}, 82$	$31, \mathbf{152}, 588$	$128, \mathbf{308}, 588$
$\Delta t_{\mathrm{SC,min}} = t_{\mathrm{min\ disr}} - t_{\mathrm{SC}}$ (ms)	$1.1, \mathbf{1.9}, 4.6$	$2.1, \mathbf{6.3}, 14$	$7.0, \mathbf{77}, 480$	$6.0, \mathbf{18}, 191$

Table 6: Intervals Δt_{SC} (first row) compared to $\Delta t_{\mathrm{SC,min}}$ for the four devices. The median values are shown in bold, as well as the first and third quartile over the database.

Figure 4a shows an example from a disruptive AUG shot of the time trace of the mode amplitude B_{r} measured by the saddle coils. The mode amplitude at the time of disruption t_{disr} will be denoted by $B_{\mathrm{r,disr}}$. It is important to note that $B_{\mathrm{r,disr}}$ was calculated in the discharge post-processing (predictions of the disruptive mode amplitude will be addressed in Section 4). Here, we can see that by setting a threshold at 50% of $B_{\mathrm{r,disr}}$, the PCS would have had a relatively long time, noted as TtD_{50}, to react. In general, we define TtD_X as the duration until t_{disr} from the chronologically *first* point where B_{r} crosses a threshold of $X\%$ of $B_{\mathrm{r,disr}}$. In the particular case in Figure 4a, the mode locks at around $t = 1.535$ s and the steep amplitude growth during the time interval ~ 1.535 s – 1.540 s is probably related to the reduction of wall shielding as the mode passes to the locked phase. At this point, we note again that for rotating modes the measured signal amplitude can deviate from the true size of the mode, depending on characteristics of the wall and the saddle coils. Hence, it is important to keep in mind that the entire analysis is based on the *measured* signal amplitudes.

For all database entries, the durations TtD_{10}, TtD_{50} and TtD_{90} were calculated, as indicated in Figure 4a. Now, in order to get an estimate, for each device, of what fraction of discharges (FD) in the database would in principle be detected at a specific time before t_{disr}, using a certain detection threshold (here 10%, 50% and 90% of $B_{\mathrm{r,disr}}$), we constructed *time-to-disruption curves*. These curves are displayed in Figure 4b for the four devices and each of the three detection thresholds (cases where even the lowest threshold was never reached before t_{disr} were excluded from the analysis). For instance, in AUG one can notice that, when setting the detection threshold at 10% of $B_{\mathrm{r,disr}}$, 90% of the disruptions would have been detected at about 3.5 ms before the time of disruption. Of course, many among those would be detected earlier, but only 50% of all AUG shots would have been detected at a TtD ~ 7.5 ms. Setting the threshold higher, to 50% of $B_{\mathrm{r,disr}}$, would deteriorate the detection results: to reach a success rate of 90% of the cases in AUG, one would have only 1 ms until the disruption, while a success rate of 50% would be feasible at about 6 ms prior to t_{disr}. Furthermore, the black curves in Figure 4b represent the fraction of database entries from each device for which the saddle coil signal duration Δt_{SC} equals the corresponding time on the horizontal axis. In COMPASS, a hard limit on Δt_{SC} is set by the pulse length, which does not exceed 1 s. The time point $t_{\mathrm{PCS}} = 10$ ms has been indicated in particular, as it represents the typical time scale of exception handling required by the PCS in large devices [5, 38]. For example, it can be seen that in JET, nearly all modes in the database can be detected by the saddle coils at a TtD exceeding t_{PCS}, while almost 80% of the modes attain a level of 10% $B_{\mathrm{r,disr}}$ before t_{PCS}.

In Figure 4c, a vertical cross-section of Figure 4b is shown for $\mathrm{TtD} = t_{\mathrm{PCS}}$, plotted against the minor radius of the four devices in the database. In general, the fraction of disruptions detected is seen to increase with plasma size—an observation that can also be deduced from Figure 4b for other values of TtD. In fact, the figure suggests that in ITER ($a = 2$ m) the vast majority of modes should have reached the level of 90% $B_{\mathrm{r,disr}}$ at least 10 ms before the disruption.

Figure 4d shows three horizontal cross-sections of Figure 4b, plotting the TtD against minor radius for a fraction of detected disruptions of 10%, 50% and 90%. The vertical spread (logarithmic) of the points from each particular device provides an idea of the typical mode

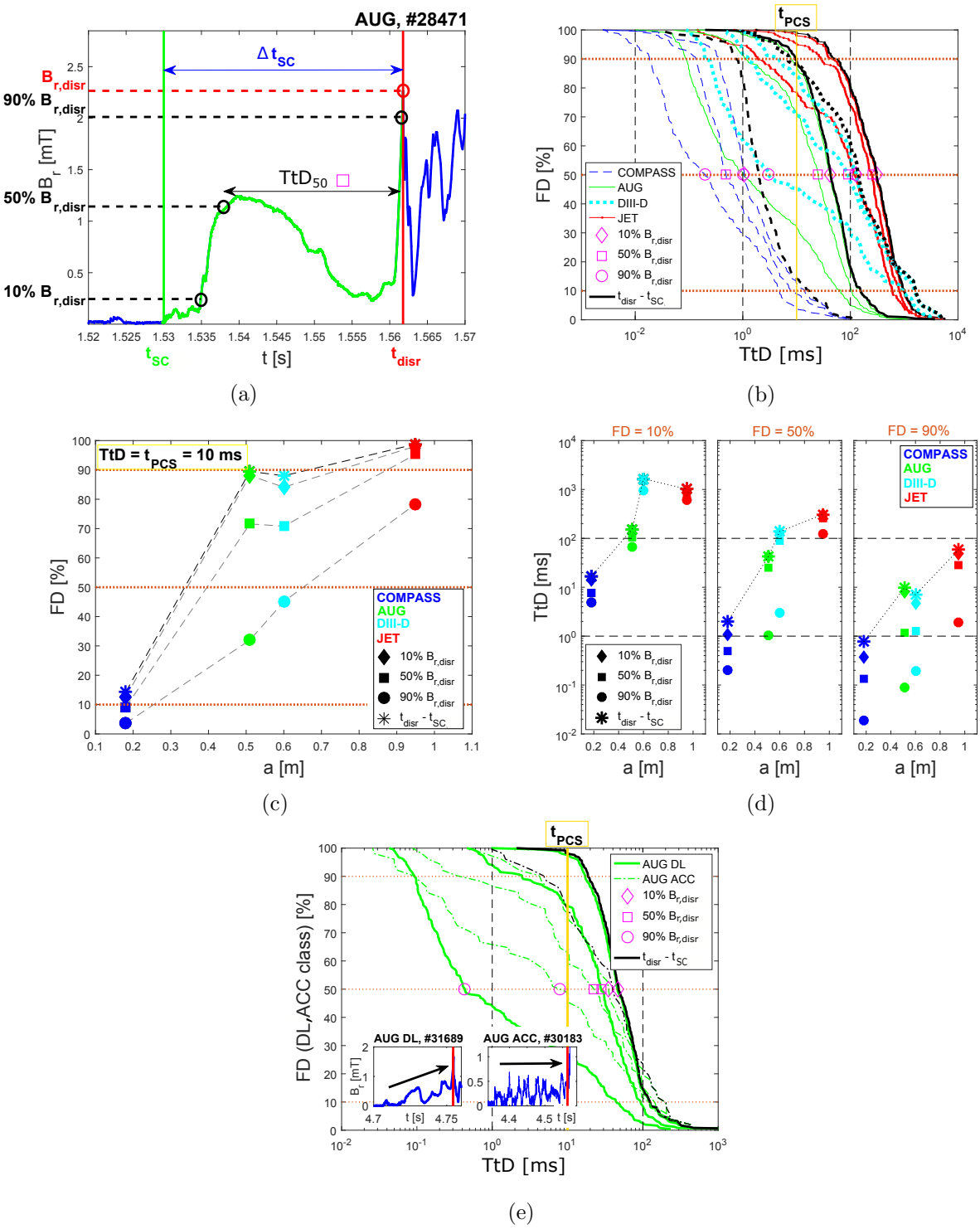

Figure 4: (a) Time trace of the mode amplitude B_r in AUG discharge #28471, with an initially rotating locked mode disrupting at $t_\mathrm{disr} \sim 1.562$ s. The mode amplitude $B_\mathrm{r,disr}$ at the time of disruption is indicated, the corresponding 10%, 50% and 90% threshold levels and TtD_{50}. (b) TtD curves obtained from the database of the four devices for the three chosen threshold levels, as well as the curves (black) corresponding to Δt_SC. (c) Vertical cross-section of (b), showing the FD values at $\mathrm{TtD} = t_\mathrm{PCS} = 10$ ms. (d) Horizontal cross-sections of (b), showing the TtD for FD = 10%, 50% and 90%. (e) TtD curves obtained from AUG discharges in the DL and ACC classes, with typical mode dynamics in the figure insets.

growth nature. The points in the panel FD = 10% (having a long TtD) are spread relatively closely, suggesting a rather flat, quasi-stable mode amplitude development. On the other hand, at FD = 90% the spread is considerably larger due to the presence of cases with a steep initial growth, followed by a quasi-stable locked phase, ending by another steep growth prior to the major disruption.

Finally, Figure 4e confirms the earlier observation that the mode growth nature depends to a certain extent on disruption class. In particular, the TtD curves for the AUG discharges in the DL and ACC groups are plotted. For example, in the DL class $\sim 50\%$ of the modes reach the threshold level of 90% $B_{\mathrm{r,disr}}$ less than a millisecond before the major disruption, whereas both the 50% and 10% levels are attained much earlier (see the typical example in the inset). In case of the ACC class, however, the difference between the TtD corresponding to distinct threshold levels is smaller, suggesting a relatively quasi-stable development with multiple peaks. The mode growth in the DL class may be driven by the relatively large increase in this class of l_{i}/q_{95} from t_{SC} to t_{disr}, which is much more limited in the ACC class [19].

3.2 Locked phase duration Δt_{LP}

We now proceed with a characterization of the second time scale focused on in this work, i.e. the locked phase duration Δt_{LP} for the modes with IRLM and BLM dynamics. This is expected to be determined mainly by the physics of mode growth and its interaction with the vacuum vessel, and, in comparison with Δt_{SC}, less by the details of the machine and diagnostics [19]. It therefore appears feasible to establish its dependencies through a scaling relation, which can serve as a design guideline for plasma control aimed at disruption avoidance and prediction.

Regression analysis was carried out using a power law model for Δt_{LP}, as it was found to fit the data considerably better than a linear model. In addition, logarithmic transformation of the data was seen to result in homogeneous variance of the residuals (homoscedasticity). All data used for regression was obtained from the start of the locked phase. An automatic feature selection technique was used to identify the optimal set of predictor variables. In particular, stepwise linear regression was applied to the log-transformed data, using the Bayesian information criterion (BIC). A feature selection technique based on a random forest resulted in the same set of predictor variables, but the power law model was preferred on account of its simplicity and ease of extrapolation. Furthermore, a more complex model with a greater number of fitting parameters is more vulnerable to overfitting, which may complicate generalization to unseen data sets. As a result of the feature selection, the following model was obtained:

$$\Delta t_{\mathrm{LP}} = \alpha_0 \, a^{\alpha_a} \, \beta_{\mathrm{N}}^{\alpha_{\beta_{\mathrm{N}}}} \, q_{95}^{\alpha_{q_{95}}} \, f_{\mathrm{rad}}^{\alpha_{f_{\mathrm{rad}}}}, \tag{4}$$

with Δt_{LP} in s, a in m and $f_{\mathrm{rad}} = P_{\mathrm{rad}}/P_{\mathrm{IN}}$ the radiated fraction, i.e. the ratio of radiated power over total input power. Two possibilities were tested: either the factor α_0 was allowed to depend on the disruption class, or it was taken as common to all classes. On a logarithmic scale, the first possibility corresponds to a class-dependent offset of the scaling, hence taking into account at least part of the variability of Δt_{LP} between classes. In both cases, the other parameters α_a, $\alpha_{\beta_{\mathrm{N}}}$, $\alpha_{q_{95}}$ and $\alpha_{f_{\mathrm{rad}}}$ were common to all classes.

Table 7 presents the results of weighted least squares regression using a subset of the database consisting of, in total, 761 IRLM and BLM cases from COMPASS (104 points, noting that the Δt_{LP} measurements from the HFS and LFS coils are similar), AUG (308), DIII-D (107) and JET (242). In order to balance the contributions from the various machines, weight factors were used for each sample i, given by $w_{ij}^{-1} = 2 + \sqrt{N_j}/4$, where N_j is the number of points contributed by device j [39]. Whether a common offset is used among all disruption classes, or a class-dependent offset, a clear trend is observed of Δt_{LP} in terms of minor radius

Common offset	α_0	α_a	α_{β_N}	α_{q95}	$\alpha_{f_{rad}}$	$\widehat{\Delta t}_{LP,ITER}$ (ms)	MdAPE (%)	RMSE (ms)	R^2
	37 ±12	3.25 ±0.14	−0.401 ±0.079	1.21 ±0.25	−0.273 ±0.038	1270 ±320	20	1.5	0.61
Class offset	$\alpha_{0,ACC}$	$\alpha_{0,BLIM}$	$\alpha_{0,DL}$	$\alpha_{0,IMP}$	$\alpha_{0,LON}$	$\alpha_{0,LOQ}$	$\alpha_{0,NBIOFF}$	$\alpha_{0,NTM}$	$\alpha_{0,RU}$
	74 ±24	29 ±13	47 ±16	18.0 ±5.8	134 ±44	38 ±14	75 ±26	83 ±27	380 ±130
		α_a	α_{β_N}	α_{q95}	$\alpha_{f_{rad}}$	$\widehat{\Delta t}_{LP,ITER}$ (ms)	MdAPE (%)	RMSE (ms)	R^2
		3.53 ±0.13	−0.189 ±0.078	1.12 ±0.26	−0.177 ±0.036	1880 ±470	19	1.3	0.70

Table 7: Results of power-law regression using weighted least squares for the locked phase duration Δt_{LP}, assuming either a common offset across all disruption classes, or a class-dependent offset. Along with parameter estimates, predictions and their error bars (one standard deviation), the median absolute percentage error (MdAPE) and root-mean-square error (RMSE) are mentioned as measures of goodness-of-fit, as well as the coefficient of determination R^2 as a measure of data variability explained by the model.

and safety factor. In addition, there may be a weak dependence of the observed Δt_{LP} on β_N and f_{rad}. A prediction $\widehat{\Delta t}_{LP}$ was made for an ITER scenario ($a = 2$ m) with $\beta_N = 1.8$, $q_{95} = 3$ and $f_{rad} = 0.5$ [40–42]. The predicted values, $\widehat{\Delta t}_{LP,ITER}$, are shown in the table. In the case of a class-dependent offset, we chose the DL class for making a prediction, because of its relatively high occurrence in the database. Predictions for other classes can be readily obtained by adjusting the multiplication factor.

It should be noted that the error bars (standard deviations) on the parameter estimates and predictions are relatively large. This also follows from the overall median absolute percentage error (MdAPE) of about 20%. Moreover, the rather low coefficient of determination R^2 indicates that the model is able to explain only part of the variability of the data. This is also apparent from the plots of the predictions $\widehat{\Delta t}_{LP}$ for all points against their experimental value Δt_{LP}, shown in Figure 5. Sources of uncertainty can be related to the occurrence of minor disruptions, a rapid sequence of initially rotating and fast locking modes (observed often in AUG density limit disruptions), changes in the mode structure, intentional variation of the plasma parameters, etc. Nevertheless, the results also reveal that the model with the class-dependent offset provides a better fit than the one with the common offset, particularly for the COMPASS data.

Concentrating on the clearest individual results in Table 7, it first becomes apparent that Δt_{LP} can vary significantly among the various disruption classes. A similar conclusion was already drawn from Table 5 for Δt_{SC}. Again, the longest locked phase durations are generally found in the LON and RU classes, while the shortest locking phases tend to occur in the IMP, BLIM and LOQ classes.

Furthermore, the increasing trend of Δt_{LP} with plasma size (minor radius a), which was also observed for Δt_{SC}, was already illustrated in Figure 2a and the scaling quantifies this dependence. In addition, still from Figure 2a, it appears that the ratio $\Delta t_{LP}/\Delta t_{SC}$ follows a similar increasing trend, indicating that the relative duration of the locking also becomes longer with increasing plasma size. In COMPASS, modes are typically found locked during about a quarter of the time over which they can be observed using the saddle coils. On the other hand, in DIII-D and JET the modes are either found locked at the time of detection, or they lock almost immediately. These differences are influenced by the physics driving the

Common offset	α_0	α_a	α_{β_N}	$\alpha_{q_{95}}$	$\alpha_{f_{rad}}$	$\widehat{\Delta t}_{LP,ITER}$ (ms)	MdAPE (%)	RMSE (ms)	R^2
	8.0 ±3.5	2.72 ±0.28	−0.90 ±0.13	2.00 ±0.41	−0.305 ±0.070	345 ±130	13	1.4	0.55
Class offset	$\alpha_{0,ACC}$	$\alpha_{0,BLIM}$	$\alpha_{0,DL}$	$\alpha_{0,IMP}$	$\alpha_{0,LON}$	$\alpha_{0,LOQ}$	$\alpha_{0,NBIOFF}$	$\alpha_{0,NTM}$	$\alpha_{0,RU}$
	31 ±14	32 ±18	28 ±14	6.7 ±3.1	47 ±22	17.1 ±8.7	36 ±18	45 ±23	158 ±85
		α_a	α_{β_N}	$\alpha_{q_{95}}$	$\alpha_{f_{rad}}$	$\widehat{\Delta t}_{LP,ITER}$ (ms)	MdAPE (%)	RMSE (ms)	R^2
		2.97 ±0.25	−0.63 ±0.12	1.31 ±0.45	−0.230 ±0.067	749 ±270	13	1.2	0.67

Table 8: Similar to Table 7, but restricted to the BLM cases.

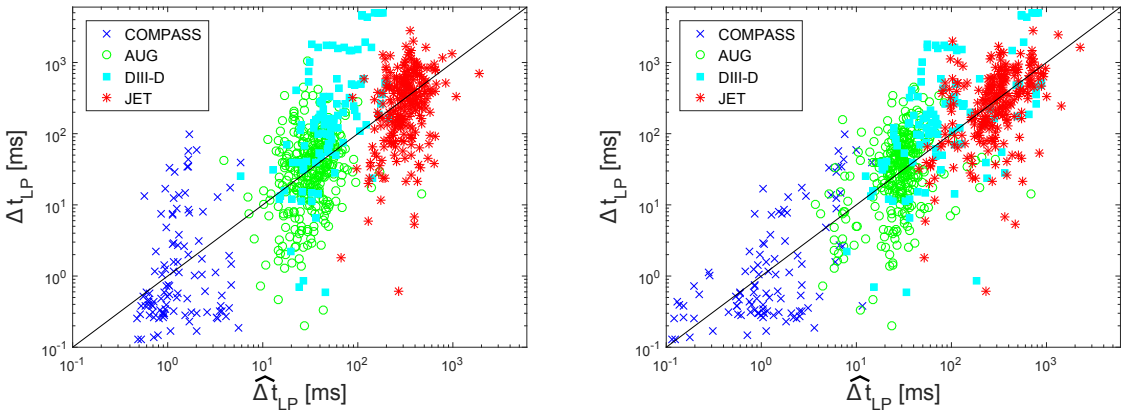

Figure 5: Predicted locked phase durations $\widehat{\Delta t}_{LP}$ against experimental values Δt_{LP} obtained from power law scaling with (a) a common offset for all classes and (b) a class-specific offset.

locking, including properties of the conducting structures surrounding the plasma (e.g. wall characteristic time τ_{w}) [19], as well as various properties of the saddle coils, like sensitivity and location. Figure 2b shows that the distribution of Δt_{LP} is quite broad and skewed, similar to the case of Δt_{SC}, corroborating the results obtained by the scaling analysis.

In addition, the locked phase duration scales positively with q_{95}. This can be understood because for larger edge safety factor the rational surface where the mode occurs is located closer to the plasma core region. The role played by the distance between the mode and the plasma edge in disruption onset was discussed more specifically in [43], where it was shown that a smaller distance increases the likelihood of disruption.

A similar regression analysis using the same approach and model was applied to the BLM cases only. In total, 259 database points were used from COMPASS (7 points), AUG (88), DIII-D (57) and JET (107), and the results are shown in Table 8. There are a number of notable differences with the results using both the IRLM and BLM points. The dependence on a has become somewhat weaker, although this may be related to the concomitant increased negative dependence on β_{N}, as a and β_{N} are quite strongly anti-correlated across the database (correlation coefficient -0.51). Furthermore, the offsets are considerably lower than in the combined case with IRLM and BLM points, contributing to a significantly lower prediction for ITER.

4 Mode amplitude scaling

Like the scaling for the locked phase duration derived in the previous section, a scaling law for the critical mode amplitude $B_{\mathrm{r,disr}}$ at the disruption onset can contribute to portability of disruption prediction schemes. In addition, the mode growth analysis in Section 3.1.5 hinges on *a posteriori* knowledge of $B_{\mathrm{r,disr}}$, whereas, of course, in reality this is not known prior to the disruption. In [9], the following empirical scaling for the experimentally measured $B_{\mathrm{r,disr}}$ was derived:

$$B_{\mathrm{r,disr}}(r_{\mathrm{c}}) = (8.5 \pm 2.5)\, I_{\mathrm{p}}^{1.07\pm0.11}\, a^{-1.1\pm0.14}\, q_{95}^{-1.2\pm0.12}\, l_{\mathrm{i}}^{1.2\pm0.12}\, \rho_{\mathrm{c}}^{-2.8\pm0.3}. \tag{5}$$

Here, $r_{\mathrm{c}} = |R_{\mathrm{geo}} - R_{\mathrm{SC}}|$ denotes the position of the saddle coils with respect to the geometric axis of the torus and $\rho_{\mathrm{c}} = |R_{\mathrm{mag}} - R_{\mathrm{SC}}|/a$ is the position with respect to the magnetic axis, normalized to a. The scaling was derived using data from COMPASS (2×19 points from HFS and LFS), AUG (35) and JET with the ITER-like wall (250), all taken at the time of the thermal quench. Rather than re-estimating the scaling using the database compiled in this work, here the original critical mode amplitude scaling (5) is validated.

It should first be noted that the accuracy of the magnetic equilibrium reconstruction, which is essential for calculating the scaling quantities, can be compromised when approaching the thermal quench, particularly during highly dynamic discharge phases comprising changes in the plasma shape, i.e. during the plasma current ramp-down or ramp-up. This led us to discard 17% of the DIII-D database entries for the analysis, leaving a total of 1086 points from all devices. Figure 6a shows the plot of the experimental critical mode amplitude $B_{\mathrm{r,disr}}$ against the predictions $\hat{B}_{\mathrm{r,disr}}$ obtained by scaling (5) for the IRLM and BLM cases (the prediction for ROT dynamics is worse; see below). The fit is reasonable, but the spread of the data is significant, as indicated also by the distribution of the ratio $B_{\mathrm{r,disr}}/\hat{B}_{\mathrm{r,disr}}$ for the pulses with IRLM and BLM mode dynamics in Figure 6b. Table 9 presents the median of the ratio $B_{\mathrm{r,disr}}/\hat{B}_{\mathrm{r,disr}}$, together with its median absolute deviation (MAD), calculated for subsets corresponding to different mode dynamics and devices. Despite the large scatter, it is clear that the predictions from the scaling law are better for the IRLM and BLM cases than for ROT dynamics, where the scaling tends to overestimate the experimental mode amplitude significantly. As mentioned in Section 2.2, this is likely due to attenuation of the measured

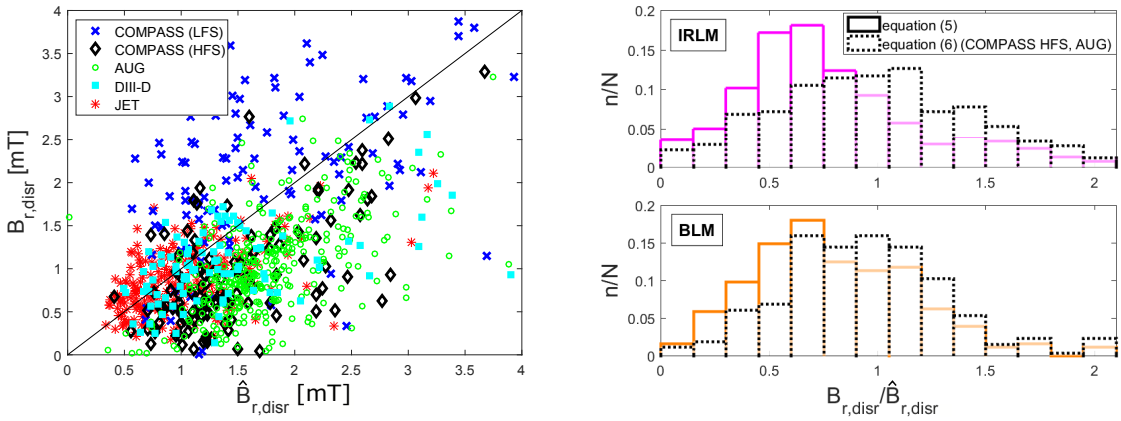

(a) (b)

Figure 6: (a) Experimental critical mode amplitude $B_{\mathrm{r,disr}}$ against the predictions, $\hat{B}_{\mathrm{r,disr}}$, obtained with scaling (5) for modes with IRLM or BLM dynamics. (b) Distributions of $B_{\mathrm{r,disr}}/\hat{B}_{\mathrm{r,disr}}$ for IRLM and BLM, obtained using scaling (5) (COMPASS LFS, DIII-D, JET) or (6) (COMPASS HFS, AUG).

Device	Mode dynamics	Scaling (5)	Scaling (6)
All	ROT	0.32 ± 0.35	0.44 ± 0.42
	IRLM	0.70 ± 0.90	1.00 ± 0.44
	BLM	0.75 ± 0.31	0.95 ± 0.32
COMPASS (HFS)	All	0.24 ± 0.56	0.40 ± 0.60
COMPASS (LFS)		0.74 ± 0.67	
AUG		0.50 ± 0.53	0.95 ± 0.42
DIII-D		0.75 ± 0.32	
JET		0.84 ± 0.33	
COMPASS (HFS)	IRLM + BLM	0.54 ± 0.29	1.05 ±0.60
COMPASS (LFS)		1.15 ± 0.60	
AUG		0.57 ± 0.20	1.05 ±0.38
DIII-D		0.83 ± 0.29	
JET		0.86 ± 0.32	

Table 9: Median ratio $B_{\mathrm{r,disr}}/\hat{B}_{\mathrm{r,disr}}$ ± MAD, for various mode dynamics and devices, obtained using scaling (5) or (6) (only for COMPASS HFS, AUG).

amplitude during mode rotation. The comparison between devices is therefore also shown in Table 9 for the IRLM and BLM cases in particular.

Comparing the scaling between the various devices, it turns out that the median fit is relatively good for the measurements obtained from the LFS coils in COMPASS, as well as those from DIII-D and particularly JET, although the spread is considerable, especially for COMPASS at the LFS. On the other hand, the scaling considerably overestimates the amplitudes measured at the HFS in COMPASS and in AUG. One probable explanation is that most of the data used for originally deriving the scaling were obtained from JET and most of the entries from JET in our database are exactly those. The fact that, together with the COMPASS HFS cases, the measurements at AUG are also obtained from coils located at the inboard side of the torus, suggests that the measurement location needs to be taken into account. Indeed, the factor $\rho_{\rm c}^{-2.8}$ in (5) relates the mode amplitude at the rational surface with the measured value at position $r_{\rm c}$ [9]. For a given mode number m, this factor should be $\sim \rho_{\rm c}^{-|m|-1}$, hence the average dominant mode number in the database used for deriving (5) was $m = 2$ [9]. However, to take into account coupling of modes with different m in a toroidal geometry, the mode number m needs to be replaced by an effective mode number $m_{\rm eff}$. A semi-analytical model used in [19, Appendix A.2] showed that, whereas only a minor correction is required at the LFS (where most of the data were obtained for deriving (5)), at the HFS a mode number $m = 2$ corresponds to a value $m_{\rm eff} = 3.8$, or a factor $\rho_{\rm c}^{-4.8}$ in (5). Hence, for the points from COMPASS at the HFS and from AUG, the following scaling relation was applied as an alternative to (5):

$$B_{\rm r,disr}(r_c) = 8.5\, I_{\rm p}^{1.07}\, a^{-1.1}\, q_{95}^{-1.2}\, l_{\rm i}^{1.2}\, \rho_{\rm c}^{-4.8}. \tag{6}$$

The resulting median ratios $B_{\rm r,disr}/\hat{B}_{\rm r,disr}$ are listed in Table 9. There is a clear improvement of the median ratio in comparison with the results from (5) (see also Figure 6b), although for the COMPASS LFS points this is only so when excluding the ROT cases. Therefore, in the remainder of this section, scaling (6) is used for COMPASS at the HFS and for AUG. With this, it is seen that the mode amplitude scaling overall provides reasonable predictions of $B_{\rm r,disr}$, with the exception of the COMPASS points, where the MAD is 0.60. It is also worth mentioning that, using (5) or (6) depending on the case, the median ratio for all data points in each of the disruption classes is seen to lie between 0.70 and 0.90 (except for a ratio of ~ 0.15 in the BLIM class). Hence, the disruption root cause seems to play a minor role in the prediction of the critical mode amplitude.

Equipped with an assessment of the confidence of the scaling predictions for the critical mode amplitude, we now focus on the TtD curves based on those predictions. Accordingly, TtD_X is defined as the duration until $t_{\rm disr}$ from the first point where $B_{\rm r}$ reaches a level of $X\%$ of $\hat{B}_{\rm r,disr}$, using the predicted rather than, as in Section 3.1.5, the experimental critical mode amplitude. An example is shown in Figure 7a, including the time traces of the predicted $\hat{B}_{\rm r,disr}$, as well as its corresponding 10%, 50% and 90% traces and TtD_{50}. It is important to note that the prediction $\hat{B}_{\rm r,disr}(t)$ at time t is based on the value of the predictor variables at the same time. In a realistic setting, this would correspond to real-time predictions from the scaling law. Figure 7b displays the TtD curves for the various devices, based on the predicted critical levels. In Figure 7c, a vertical cross-section is plotted of panel (b), at a time right before the disruption where the maximum fraction of disruptions would have been captured in the various devices at the respective threshold levels. The best performance is seen in JET and AUG, whereas in DIII-D the 90% level curve intersects the $B_{\rm r}$ experimental time traces in less than 40% of the examined cases prior to the major disruption onset. In addition, Figure 7d shows a similar vertical cross-section of panel (b), but now for a typical PCS reaction time $t_{\rm PCS} = 10$ ms. Comparing with the analysis based on the experimental value of $B_{\rm r,disr}$, Figure 4c, it is seen that overall the performance in terms of fraction of detected disruptions is relatively similar, except for DIII-D and the 10% level in JET. It

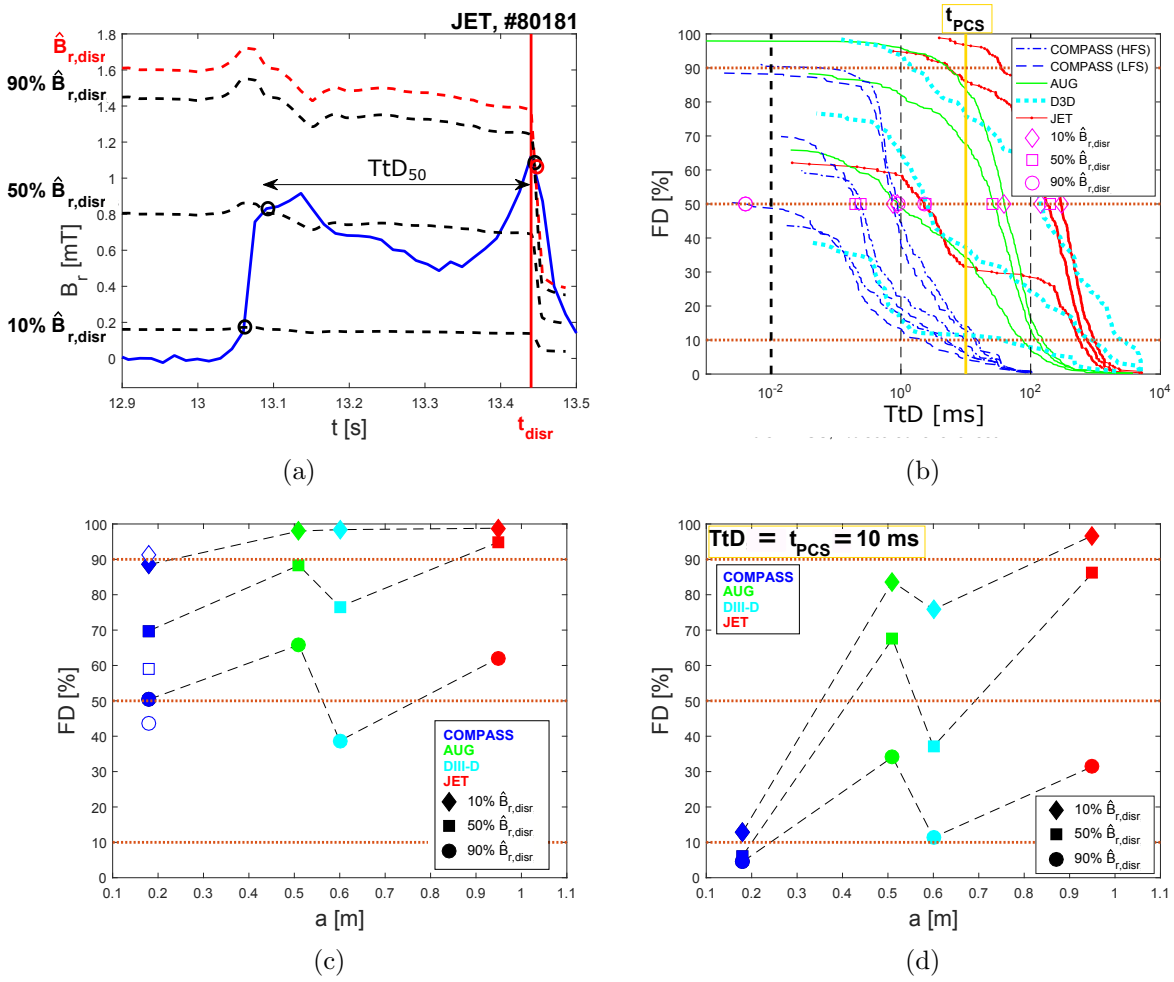

Figure 7: (a) Time trace of the mode amplitude B_r in JET pulse #80181, which disrupted due to a locked mode $t_\mathrm{disr} \sim 13.440$ s. The time evolution of the predictions $\hat{B}_\mathrm{r,disr}$ are also shown, as well as the corresponding 10%, 50% and 90% traces and TtD_{50}. The point at which $\hat{B}_\mathrm{r,disr}$ intersects the experimental B_r time trace is indicated with a red circle. (b) TtD curves obtained from the database for the four devices, corresponding to the three threshold traces, based on the predictions $\hat{B}_\mathrm{r,disr}$. (c) Vertical cross-section of (b), showing the maximum FD values reached prior to the disruption. (d) Cross-section of (b) at $t_\mathrm{PCS} = 10$ ms. For COMPASS, only LFS data points are shown (HFS data points are very similar).

was also noted, as one would expect, that the highest detection performance was attained in the LON and RU classes, which were earlier seen to exhibit overall the longest locked phase durations. Accordingly, the lowest performance was reached in the IMP, BLIM and IMP, with generally the shortest locked phases.

5 Discussion and conclusions

In ITER, the boundaries of the non-disruptive operational space will be explored extensively, yet ITER will be able to sustain only a limited number of disruptions [1]. Therefore, an important asset of the database developed in this work is its great diversity in terms of device characteristics, operational conditions, mode dynamics and disruption root causes. The time scales of the observed modes in the database extend over several orders of magnitudes. In addition, a multitude of factors was identified that influence the dynamics of MHD modes acting as disruption precursors. The effect of some of these factors on the mode characteristics could be quantified using an empirical scaling, be it with considerable uncertainty on the predictions. Other effects were merely identified and roughly characterized, possibly depending on too complex physical or technical details of the plasma, the device and the diagnostics to allow more detailed quantification with the simple models used in this work. Nevertheless, it is fair to assume that solutions for control in ITER, aimed at avoidance and mitigation of disruptions, will have to cope with the practical issue of substantial uncertainty of the diagnostic input on which the control system will need to base its decisions. We here argue that a reliable approach to disruption avoidance, prediction and mitigation in tokamaks on the one hand has to be based on robust trends of the characteristics of disruption precursors in terms of plasma conditions, emerging from physical models or empirical scalings using simple statistical models. On the other hand, the unavoidably remaining degree of uncertainty may need to be addressed with proper decision logic that can handle this uncertainty, e.g. by relying on probabilistic models, fuzzy logic, machine learning, etc. The present work is related to the former aspect of this combined approach, by establishing guidelines and boundary conditions for plasma control in response to MHD precursors to disruptions and by quantifying the main trends of MHD mode characteristics as a function of a limited number of plasma parameters.

In this work, a database was compiled with entries from more that 1 100 discharges that terminated in a disruption, originating from four tokamaks of varying size, and fully classified according to disruption root cause [2]. The database provides a solid basis for analysis of MHD precursors of both major and minor disruptions. In this paper, the time Δt_{SC} during which a mode can be observed using saddle coils was characterized across devices, together with the duration of the locked phase Δt_{LP}. Various factors were identified that influence these time scales and a scaling law for Δt_{LP} was established. Furthermore, an earlier scaling law for the mode amplitude at the disruption onset was validated using the compiled database.

Characteristics of both time scales Δt_{SC} and Δt_{LP} studied in this paper constitute important input to plasma control seeking for preemptive action in relation to disruptions. Our database study has revealed a substantial fraction of rotating modes leading to a disruption, without ever having become locked to the vessel. It has been shown before that rotating modes can be missed by device protection schemes and induce a major disruption [19]. On the other hand, we have also noted that the ratio $\Delta t_{\mathrm{LP}}/\Delta t_{\mathrm{SC}}$ approaches unity in the larger devices (DIII-D and JET). Following this trend to ITER, one would expect almost all modes to be found locked upon detection in that device, prior to the disruption, particularly in the case of low plasma rotation [19]. Nevertheless, care has to be taken with such extrapolations, because additional factors can also play a role in determining whether a mode will experience a (substantial) rotational phase prior to locking. Apart from intrinsic and extrinsic sources of plasma rotation, this includes the intensity of error fields, discharge scenario, etc. As a

result, it is recommended to monitor not only locked but also rotating modes with a view to device protection, also in large devices.

Generally speaking, a clear increasing trend of the time scales Δt_{SC} and Δt_{LP} was seen with plasma size, indicating that, in large devices, the plasma control system (PCS) typically has more time to react to MHD mode disruption precursors than in the smaller ones. Specifically, the scaling law for Δt_{LP} suggests a locked phase duration of several hundreds of milliseconds to seconds at $q_{95} = 3$ in ITER, increasing about linearly with the edge safety factor. The shortest prediction is for born-locked modes, but also that is still of the order of 100 ms. However, it was also found that both Δt_{SC} and Δt_{LP} can vary significantly depending on the disruption root cause. Modes due to impurity-induced radiative collapse, the β limit and low edge safety factor typically evolve on a relatively short time scale, whereas modes triggered due to error fields at low density or by too fast a current ramp-up tend to be much slower. Complicating the extrapolation to ITER is the strong variation of the relative occurrence of disruption causes among devices. In addition, it is clear that a differentiated response of the PCS according to disruption root cause presupposes reliable means to establish that root cause in real time during plasma operation.

The extrapolations of the relevant time scales to ITER may be compared to the minimum required reaction time of ITER's disruption mitigation system of about 30 ms [24]. However, recalling the danger of false positive alarms in disruption prediction, another essential ingredient for assessing the disruption risk due to an MHD mode is its size, usually gauged by the amplitude of the radial component B_{r} of the associated magnetic field, measured at the position of the saddle coils. To that end, the scaling law for the mode amplitude $B_{\mathrm{r,disr}}$, first developed in [9], can serve as a useful instrument. After correction for the situation with saddle coils located on the inboard side of the torus, the scaling was seen to provide reasonable predictions of $B_{\mathrm{r,disr}}$. One important possible source of prediction uncertainty is related to the equilibrium reconstruction approaching the thermal quench. In addition, systematic overestimation of $B_{\mathrm{r,disr}}$ in the case of rotating modes may be due to attenuation of B_{r} as a result of wall currents. A reliable technique to compensate for these wall currents would allow to obtain, in real time, a better estimate of the actual mode amplitude during mode braking [44].

By constructing time-to-disruption (TtD) curves, a rough estimate was obtained over the entire database of the fraction of disruptions that would trigger a warning by a specific time before the disruption (e.g. the PCS actuation time), for a given threshold level of the mode amplitude. Relatively similar results were observed using either the experimentally measured $B_{\mathrm{r,disr}}$ (not available in a realistic setting) or the prediction from the amplitude scaling that was validated in this work. It should be noted that, at this point, the TtD curves are intended to serve for demonstration purposes, not for providing a direct indication of the success rate in a realistic disruption prediction scheme. For instance, setting the threshold level at 10% of $B_{\mathrm{r,disr}}$ (measured experimentally or predicted by the scaling law) would allow capturing almost all JET disruptions in the database at least 10 ms in advance, but it would also lead to many false positive results. One possible type of events that may trigger a false alarm are minor disruptions, which tend to become more probable as the duration of the mode increases and are therefore quite often observed in the larger devices (where they may represent a threat themselves, on even shorter time scales). Nevertheless, TtD curves are a convenient instrument for quantifying overall mode dynamics in a large database, with the possibility to differentiate between disruption classes, as a useful alternative to analytical or numerical modeling approaches. In addition, a favorable overall trend of the fraction of detected disruptions was again observed with increasing plasma size. Simple extrapolation of this trend suggests that, in ITER, at least 10 ms before the disruption almost all modes will have reached an amplitude of 90% $B_{\mathrm{r,disr}}$—a level at which the risk of false alarms is presumably acceptable.

The database constructed in this work can also serve for applying a similar analysis, including TtD curves, to quantities other than the mode lock amplitude, such as the ratio l_i/q_{95}, radiated power, normalized pressure β, plasma density, etc. Eventually, this may contribute to the development of a multi-threshold disruption predictor. However, given the substantial uncertainty on some of the results presented in this work, such as the predictions of the scaling laws, it is well possible that a similar approach applied to multiple quantities would still leave some degree of uncertainty of a disruption forecast. Hence, considering the severe limitation on the acceptable number of unmitigated disruptions in the ITER high performance scenario, the work presented here could also be used to constrain more complex models, such as neural networks [45].

Acknowledgements

The authors would like to acknowledge helpful input from M. Maraschek, O. Kovanda, E. Strait and M. Baruzzo and other members of the involved tokamak teams. This work has been carried out within the frameworks of the EUROfusion Consortium and FUSION-DC and has received funding from the Euratom research and training programme 2014–2018 and 2019–2020 under grant agreement No. 633053. The work has also been supported by project MEYS, projects LM2015045, 8D15001 and CZ.02.1.01/0.0/0.0/16_019/0000768, by US DOE under DE-FC02-04ER54698 and by the US DOE Fusion Energy Sciences Postdoctoral Research Program administered by the Oak Ridge Institute for Science and Education (ORISE) for the DOE. ORISE is managed by Oak Ridge Associated Universities (ORAU) under DOE contract number DE-SC0014664.

Disclaimer

References

[1] M. Lehnen, K. Aleynikova, P. Aleynikov, D. Campbell, P. Drewelow, N. Eidietis, Y. Gasparyan, R. Granetz, Y. Gribov, N. Hartmann, E. Hollmann, V. Izzo, S. Jachmich, S.-H. Kim, M. Kočan, H. Koslowski, D. Kovalenko, U. Kruezi, A. Loarte, S. Maruyama, G. Matthews, P. Parks, G. Pautasso, R. Pitts, C. Reux, V. Riccardo, R. Roccella, J. Snipes, A. Thornton, P. de Vries, Disruptions in ITER and strategies for their control and mitigation, Journal of Nuclear Materials 463 (2015) 39 – 48. doi:https://doi.org/10.1016/j.jnucmat.2014.10.075.

[2] P. C. de Vries, M. F. Johnson, B. Alper, P. Buratti, T. C. Hender, H. R. Koslowski, V. Riccardo, JET-EFDA Contributors, Survey of disruption causes at JET, Nuclear Fusion 51 (5) (2011) 053018. doi:10.1088/0029-5515/51/5/053018.

[3] M. F. F. Nave, J. A. Wesson, Mode locking in tokamaks, Nuclear Fusion 30 (12) (1990) 2575–2583. doi:10.1088/0029-5515/30/12/011.

[4] E. Strait, J. Barr, M. Baruzzo, J. Berkery, R. Buttery, P. de Vries, N. Eidietis, R. Granetz, J. Hanson, C. Holcomb, D. Humphreys, J. Kim, E. Kolemen, M. Kong, M. Lanctot, M. Lehnen, E. Lerche, N. Logan, M. Maraschek, M. Okabayashi, J. Park, A. Pau, G. Pautasso, F. Poli, C. Rea, S. Sabbagh, O. Sauter, E. Schuster, U. Sheikh, C. Sozzi, F. Turco, A. Turnbull, Z. Wang, W. Wehner, L. Zeng, Progress in disruption prevention for ITER, Nuclear Fusion 59 (11) (2019) 112012. doi:10.1088/1741-4326/ab15de.

[5] G. Pautasso, P. C. de Vries, D. Humphreys, M. Lehnen, C. Rapson, G. Raupp, J. A. Snipes, W. Treutterer, A. Vergara-Fernandez, L. Zabeo, The ITER disruption mitigation trigger: developing its preliminary design, Nuclear Fusion 58 (3) (2018) 036011. doi:10.1088/1741-4326/aaa137.

[6] M. Maraschek, S. Fietz, A. Gude, S. Günter, R. Koslowski, K. Lackner, K. Lüders, T. Lunt, G. Pautasso, E. Strumberger, W. Suttrop, Q. Yu, H. Zohm, Measurement and impact of the n=1 intrinsic error field at ASDEX Upgrade, 40th EPS Conference on Plasma Physics, EPS 2013 (2013) 998–1001.

[7] N. W. Eidietis, W. Choi, S. H. Hahn, D. A. Humphreys, B. S. Sammuli, M. L. Walker, Implementing a finite-state off-normal and fault response system for disruption avoidance in tokamaks, Nuclear Fusion 58 (5) (2018) 056023. doi:10.1088/1741-4326/aab62c.

[8] C. Reux, M. Lehnen, U. Kruezi, S. Jachmich, P. Card, K. Heinola, E. Joffrin, P. J. Lomas, S. Marsen, G. Matthews, V. Riccardo, F. Rimini, P. de Vries, Use of the disruption mitigation valve in closed loop for routine protection at JET, Fusion Engineering and Design 88 (6) (2013) 1101 – 1104. doi:https://doi.org/10.1016/j.fusengdes.2012.12.026.

[9] P. C. de Vries, G. Pautasso, E. Nardon, P. Cahyna, S. Gerasimov, J. Havlicek, T. C. Hender, G. T. A. Huijsmans, M. Lehnen, M. Maraschek, T. Markovič, J. Snipes, the COMPASS Team, the ASDEX Upgrade Team, JET Contributors, Scaling of the MHD perturbation amplitude required to trigger a disruption and predictions for ITER, Nuclear Fusion 56 (2) (2015) 026007. doi:10.1088/0029-5515/56/2/026007.

[10] J. Kates-Harbeck, A. Svyatkovskiy, W. Tang, Predicting disruptive instabilities in controlled fusion plasmas through deep learning, Nature 568 (7753) (2019) 526. doi:10.1038/s41586-019-1116-4.

[11] Y. Fu, D. Eldon, K. Erickson, K. Kleijwegt, L. Lupin-Jimenez, M. Boyer, N. Eidietis, N. Barbour, O. Izacard, E. Kolemen, Machine learning control for disruption and tearing mode avoidance, Physics of Plasmas 27 (2) (2020) 022501. doi:10.1063/1.5125581.

[12] B. Cannas, A. Fanni, G. Pautasso, G. Sias, P. Sonato, An adaptive real-time disruption predictor for ASDEX Upgrade, Nuclear Fusion 50 (7) (2010) 075004. doi:10.1088/0029-5515/50/7/075004.

[13] G. Rattá, J. Vega, A. Murari, G. Vagliasindi, M. Johnson, P. de Vries, JET EFDA Contributors, An advanced disruption predictor for JET tested in a simulated real-time environment, Nuclear Fusion 50 (2) (2010) 025005. doi:10.1088/0029-5515/50/2/025005.

[14] C. Rea, K. Montes, K. Erickson, R. Granetz, R. Tinguely, A real-time machine learning-based disruption predictor on DIII-D, Nuclear Fusion 59 (9) (2019) 096016. doi:10.1088/1741-4326/ab28bf.

[15] H. van den Brand, M. R. de Baar, N. J. L. Cardozo, E. Westerhof, Integrated modelling of island growth, stabilization and mode locking: consequences for NTM control on ITER, Plasma Physics and Controlled Fusion 54 (9) 094003. doi:10.1088/0741-3335/54/9/094003.

[16] A. Pau, B. Cannas, A. Fanni, G. Sias, M. Baruzzo, A. Murari, G. Pautasso, M. Tsalas, A tool to support the construction of reliable disruption databases, Fusion Engineering and Design 125 (2017) 139 – 153. doi:https://doi.org/10.1016/j.fusengdes.2017.10.003.

[17] L. E. Zakharov, S. Galkin, S. Gerasimov, Understanding disruptions in tokamaks, Physics of Plasmas 19 (2012). doi:10.1063/1.4705694.

[18] R. Paccagnella, H. R. Strauss, J. Breslau, 3D MHD VDE and disruptions simulations of tokamaks plasmas including some ITER scenarios, Nuclear Fusion 49 (3) (2009) 035003. doi:10.1088/0029-5515/49/3/035003.

[19] V. Klevarová, H. Zohm, G. Pautasso, G. Tardini, R. McDermott, G. Verdoolaege, J. Snipes, P. C. de Vries, M. Lehnen, the EUROfusion MST1 team, the ASDEX Upgrade team, Validation of a tearing mode locking model using a database of disruptive plasmas at ASDEX Upgrade, Plasma Physics and Controlled Fusion 62 (2) (2019) 025024. doi:10.1088/1361-6587/ab5c41.

[20] R. J. La Haye, R. Prater, R. J. Buttery, N. Hayashi, A. Isayama, M. E. Maraschek, L. Urso, H. Zohm, Cross–machine benchmarking for ITER of neoclassical tearing mode stabilization by electron cyclotron current drive, Nuclear Fusion 46 (4) (2006) 451–461. doi:10.1088/0029-5515/46/4/006.

[21] V. Riccardo, T. C. Hender, P. J. Lomas, B. Alper, T. Bolzonella, P. de Vries, G. P. Maddison, the JET EFDA Contributors, Analysis of JET halo currents, Plasma Physics and Controlled Fusion 46 (6) (2004) 925–934. doi:10.1088/0741-3335/46/6/001.

[22] H. Zohm, Magnetohydrodynamic stability of tokamaks, Wiley-VCH, 2015, ISBN: 978-3527412327. doi:10.1002/9783527677375.

[23] P. C. de Vries, G. Arnoux, A. Huber, J. Flanagan, M. Lehnen, V. Riccardo, C. Reux, S. Jachmich, C. Lowry, G. Calabro, D. Frigione, M. Tsalas, N. Hartmann, S. Brezinsek, M. Clever, D. Douai, M. Groth, T. C. Hender, E. Hodille, E. Joffrin, U. Kruezi, G. F. Matthews, J. Morris, R. Neu, V. Philipps, G. Sergienko, M. Sertoli, the JET EFDA Contributors, The impact of the ITER-like wall at JET on disruptions, Plasma Physics and Controlled Fusion 54 (12) (2012) 124032. doi:10.1088/0741-3335/54/12/124032.

[24] G. Pautasso, P. C. De Vries, Disruption causes in ASDEX Upgrade, 41st EPS Conference on Plasma Physics, EPS 2014 (2014) P2.015.

[25] J. Rapp, P. C. D. Vries, F. C. Schüller, M. Z. Tokar, W. Biel, R. Jaspers, H. R. Koslowski, A. Krämer-Flecken, A. Kreter, M. Lehnen, A. Pospieszczyk, D. Reiser, U. Samm, G. Sergienko, Density limits in TEXTOR-94 auxiliary heated discharges, Nuclear Fusion 39 (6) (1999) 765–776. doi:10.1088/0029-5515/39/6/305.

[26] M. Bernert, T. Eich, A. Kallenbach, D. Carralero, A. Huber, P. T. Lang, S. Potzel, F. Reimold, J. Schweinzer, E. Viezzer, H. Zohm, The h-mode density limit in the full

tungsten ASDEX upgrade tokamak, Plasma Physics and Controlled Fusion 57 (1) (2014) 014038. doi:10.1088/0741-3335/57/1/014038.

[27] F. Troyon, R. Gruber, H. Saurenmann, S. Semenzato, S. Succi, MHD-limits to plasma confinement, Plasma Physics and Controlled Fusion 26 (1A) (1984) 209–215. doi:10.1088/0741-3335/26/1a/319.

[28] J. Wesson, Tokamaks, Oxford University Press, 2011, ISBN: 978-0198562931. doi:10.1017/S0022377804003058.

[29] M. Greenwald, J. L. Terry, S. M. Wolfe, S. Ejima, M. G. Bell, S. M. Kaye, G. H. Neilson, A new look at density limits in tokamaks, Nuclear Fusion 28 (12) (1988) 2199–2207. doi:10.1088/0029-5515/28/12/009.

[30] J. A. Snipes, D. J. Campbell, P. S. Haynes, T. C. Hender, M. Hugon, P. J. Lomas, N. J. L. Cardozo, M. F. F. Nave, F. C. Schüller, Large amplitude quasi-stationary MHD modes in JET, Nuclear Fusion 28 (6) (1988) 1085–1097. doi:10.1088/0029-5515/28/6/010.

[31] R. J. La Haye, R. Fitzpatrick, T. C. Hender, A. W. Morris, J. T. Scoville, T. N. Todd, Critical error fields for locked mode instability in tokamaks, Physics of Fluids B: Plasma Physics 4 (7) (1992) 2098. doi:10.1063/1.860017.

[32] J. T. Scoville, R. J. La Haye, Multi-mode error field correction on the DIII-d tokamak, Nuclear Fusion 43 (4) (2003) 250–257. doi:10.1088/0029-5515/43/4/305.

[33] J. S. deGrassie, W. M. Solomon, J. E. Rice, J. M. Noterdaeme, Dimensionless size scaling of intrinsic rotation in DIII-D, Physics of Plasmas 23 (8) (2016) 082501. doi:10.1063/1.4960023.

[34] R. J. Buttery, M. De Benedetti, D. A. Gates, Y. Gribov, T. C. Hender, R. J. La Haye, P. Leahy, J. A. Leuer, A. W. Morris, A. Santagiustina, J. T. Scoville, B. J. D. Tubbing, JET Team, COMPASS-D Research Team, DIII-D Team, Error field mode studies on JET, COMPASS-D and DIII-D, and implications for ITER, Nuclear Fusion 39 (11Y) (1999) 1827–1835. doi:10.1088/0029-5515/39/11y/323.

[35] C. Z. Cheng, H. P. Furth, A. H. Boozer, MHD stable regime of the tokamak, Plasma Physics and Controlled Fusion 29 (3) (1987) 351–366. doi:10.1088/0741-3335/29/3/006.

[36] J. A. Wesson, R. D. Gill, M. Hugon, F. C. Schüller, J. A. Snipes, D. J. Ward, D. V. Bartlett, D. J. Campbell, P. A. Duperrex, A. W. Edwards, R. S. Granetz, N. A. O. Gottardi, T. C. Hender, E. Lazzaro, P. J. Lomas, N. L. Cardozo, K. F. Mast, M. F. F. Nave, N. A. Salmon, P. Smeulders, P. R. Thomas, B. J. D. Tubbing, M. F. Turner, A. Weller, Disruptions in JET, Nuclear Fusion 29 (4) (1989) 641–666. doi:10.1088/0029-5515/29/4/009.

[37] M. F. Turner, J. A. Wesson, Transport, instability and disruptions in tokamaks, Nuclear Fusion 22 (8) (1982) 1069–1078. doi:10.1088/0029-5515/22/8/006.

[38] K. Kurihara, J. B. Lister, D. A. Humphreys, J. R. Ferron, W. Treutterer, F. Sartori, R. Felton, S. Brémond, P. Moreau, Plasma control systems relevant to iter and fusion power plants, Fusion Engineering and Design 83 (7) (2008) 959 – 970. doi:https://doi.org/10.1016/j.fusengdes.2008.06.027.

[39] O. Kardaun, Interval estimate of the global energy confinement time during ELMy H-mode in ITER-FEAT, based on the international multi-tokamak ITERH.DB3 dataset,

IPP-IR-2002/5 1.1, Max Planck Institute for Plasma Physics, Garching, Germany (2002).
URL http://hdl.handle.net/11858/00-001M-0000-0027-40C4-1

[40] A. C. C. Sips, for the Steady State Operation and the Transport Physics topical group Activity, Advanced scenarios for ITER operation, Plasma Physics and Controlled Fusion 47 (5A) (2005) A19–A40. doi:10.1088/0741-3335/47/5a/003.

[41] A. Sips, J. Schweinzer, T. Luce, S. Wolfe, H. Urano, J. Hobirk, S. Ide, E. Joffrin, C. Kessel, S. Kim, P. Lomas, I. Nunes, T. Pütterich, F. Rimini, W. Solomon, J. Stober, F. Turco, P. de Vries, Assessment of the baseline scenario at q 95 = 3 for iter, Nuclear Fusion 58 (12) (2018) 126010. doi:10.1088/1741-4326/aade57.

[42] A. Murari, E. Peluso, P. Gaudio, M. Gelfusa, Robust scaling laws for energy confinement time, including radiated fraction, in tokamaks, Nuclear Fusion 57 (12) (2017) 26017. doi:10.1088/1741-4326/aa7bb4.

[43] R. Sweeney, W. Choi, R. J. La Haye, S. Mao, K. E. J. Olofsson, F. A. Volpe, the DIII-D Team, Statistical analysis of locked and quasi-stationary modes with rotating precursors at DIII-D, Nuclear Fusion 57 (1) (2016) 016019. doi:10.1088/0029-5515/57/1/016019.

[44] R. Sweeney, E. Strait, Decomposing magnetic field measurements into internally and externally sourced components in toroidal plasma devices, Physics of Plasmas 26 (1) (2019) 012509. doi:10.1063/1.5067321.

[45] M. Raissi, P. Perdikaris, G. Karniadakis, Physics-informed neural networks: A deep learning framework for solving forward and inverse problems involving nonlinear partial differential equations, Journal of Computational Physics 378 (2) (2019) 686. doi:10.1016/j.jcp.2018.10.045.